Materials Today Bio 18 (2023) 100541

Contents lists available at ScienceDirect

Materials Today Bio

journal homepage: www.journals.elsevier.com/materials-today-bio

Isotropic conductive paste for bioresorbable electronics

Kyung Su Kim [a,b,1], Woo-Youl Maeng [c,1], Seongchan Kim [d], Gyubok Lee [e], Minki Hong [a,b], Ga-been Kim [a,d], Jaewon Kim [a], Sungeun Kim [a,b], Seunghun Han [a,b], Jaeyoung Yoo [f], Hyojin Lee [d,g], Kangwon Lee [e,h], Jahyun Koo [a,b,*]

[a] School of Biomedical Engineering, Korea University, Seoul, 02841, South Korea
[b] Interdisciplinary Program in Precision Public Health, Korea University, Seoul, 02841, South Korea
[c] Center for Bio-Integrated Electronics, Northwestern University, Evanston, IL, 60208, USA
[d] Biomaterials Research Center, Biomedical Research Division, Korea Institute of Science and Technology (KIST), Seoul, 02792, South Korea
[e] Department of Applied Bioengineering, Graduate School of Convergence Science and Technology, Seoul National University, Seoul, 08826, South Korea
[f] Department of Materials Science and Engineering, Korea Advanced Institute of Science and Technology (KAIST), Daejeon, 34141, South Korea
[g] Division of Bio-Medical Science & Technology, KIST School, Korea University of Science and Technology (UST), Seoul, 02792, South Korea
[h] Research Institute for Convergence Science, Seoul National University, Seoul, 08826, South Korea

ARTICLE INFO

Keywords:
Isotropic conductive adhesive
Conductive paste
Implantable medical device
Biodegradable electronics
Screen printing

ABSTRACT

Bioresorbable implantable medical devices can be employed in versatile clinical scenarios that burden patients with complications and surgical removal of conventional devices. However, a shortage of suitable electrical interconnection materials limits the development of bioresorbable electronic systems. Therefore, this study highlights a highly conductive, naturally resorbable paste exhibiting enhanced electrical conductivity and mechanical stability that can solve the existing problems of bioresorbable interconnections. Multifaceted experiments on electrical and physical properties were used to optimize the composition of pastes containing beeswax, submicron tungsten particles, and glycofurol. These pastes embody isotropic conductive paths for three-dimensional interconnects and function as antennas, sensors, and contact pads for bioresorbable electronic devices. The degradation behavior in aqueous solutions was used to assess its stability and ability to retain electrical conductance (~7 kS/m) and structural form over the requisite dissolution period. *In vitro* and *in vivo* biocompatibility tests clarified the safety of the paste as an implantable material.

1. Introduction

Recently, bioresorbable electronic components have been developed for implantable medical devices that dissolve *in vivo* in a timely manner to avoid risky surgical removal [1–8]. Such devices have evolved into temporary actuators [9], energy harvesters [10,11], drug delivery systems [12], and biomarker sensors [13,14], enabling safe and short-term applications in acute, complex, and various clinical scenarios, such as peripheral nerve regeneration [9,15], oncology treatment [12,16], and intracranial hypertension detection [17,18].

When packaging bioresorbable devices, a conductive material is required to provide electrical interconnections between the components. Conventional electronics can employ solder alloys or conductive adhesives as electrical interconnection materials for bonding integrated circuits to boards. In contrast, although various composites have been suggested for bioresorbable interconnection materials [19–23], such materials are still difficult to utilize owing to their many limitations, including low electrical conductivity, poor processability, and mechanical instability. For example, when conductive polymers (CPs), such as poly (3,4-ethylenedioxythiophene) (PEDOT) and polypyrrole (PPy), are fused with bioresorbable polymers [21–23], they yield poor conductivities (<0.1 kS/m), which undermines the device electrical power and efficiency [24,25]. Furthermore, the resorption and biocompatibility of CPs are not well established [26]. For metal particles/bioresorbable polymer composites, using organic solvents or heating the matrix polymer above 200 °C damages the substrate and components at the application sites [26–28]. Although another composite comprising candelilla wax and molybdenum particles provides a relatively high conductivity of ~4 kS/m [29], candelilla wax is very brittle, making the interconnections fragile with lower mechanical stress and shortened expected lifetime of the device [30,

* Corresponding author.. School of Biomedical Engineering, Korea University, Seoul, 02841, South Korea.
E-mail address: jahyunkoo@korea.ac.kr (J. Koo).
[1] These authors contributed equally: Kyung Su Kim and Woo-Youl Maeng.

https://doi.org/10.1016/j.mtbio.2023.100541
Received 6 November 2022; Received in revised form 18 December 2022; Accepted 2 January 2023
Available online 4 January 2023

31]. Recently, bioresorbable metal particle-based conductive materials have emerged [32–35]. Sintered by laser ablation and electrochemical fusion between metal particles, such materials are equipped with high conductivity (>2 kS/m), microscale resolution, and durability under various deformation modes. Furthermore, these materials can use any substrate because they do not exploit high temperatures and toxic solvents in their application process. However, because these materials are designed for constructing planar electrical pathways, they have limitations to make physical binding and vertical interconnection. Consequently, own drawbacks of prior bioresorbable interconnection materials degrade the performance of fully bioresorbable devices or make unstable connection sites [24]. Therefore, solder or silver paste, which is not a resorbable material, is still used to prepare bioresorbable electronic device prototypes [30,36–38]. Consequently, the lack of suitable interconnections causes a discrepancy between the laboratory results and practical applications and generates a bottleneck for further research toward commercialization [39].

In this study, we used a thermoplastic beeswax matrix and glycofurol (GF) as a tungsten (W) dispersion agent to devise a highly conductive, mechanically stable, and bioresorbable W paste. The resulting material, named "W-paste", exhibited higher conductivity (>7 kS/m) and overcame the mechanical disadvantage of the existing wax composite. The W-paste can be easily prepared without cumbersome synthesis. Solidification in a few seconds by exposing room temperature is followed by screen-printing or soldering iron with manually adjustable thickness in microscale. In addition, the W-paste exhibits isotropic electrical paths, unlike the former bioresorbable interconnections, which could not retain isotropic structures [28,29,37,40]. Moreover, the W-paste can serve as conducting paths and interconnects in various applications such as antennas, flex sensors, and capacitive-fringe field sensors, as a degradation behavior was observed when immersed in phosphate-buffered saline (PBS) for 80 days. *In vitro* and *in vivo* biocompatibility tests also showed that the W-paste is nontoxic and can be used for fabricating implantable devices.

2. Materials and methods

2.1. Preparation of bioresorbable W-paste

The W particles were added to the melted beeswax (refined, *Apis mellifera*) at 100 °C to form a black mixture. After the mixture was cooled to 70 °C, GF was added and dispersed by ultrasonication to obtain the conductive W-paste. The optimal vol% varied by particle size; that is, the optimal vol% for 500 nm, 2 μm, and 10 μm W particle sizes were in ranges of 19–31%, 29–39%, and 31–41%, respectively. The paste using molybdenum (Mo) particles for the control group was prepared using the same method. The metal particles were purchased from Avention Co., Korea, and all the chemicals were purchased from Sigma–Aldrich Co., USA.

2.2. Electrical property tests

The W-paste was homogeneously mixed at 70 °C and poured into polydimethylsiloxane (PDMS) molds. After 12 h at room temperature (~21 °C), the solidified W-paste was separated from the molds and transferred onto glass slides to form disk-shaped (radius: 30 mm, thickness: 1 mm) samples for measuring the conductivity, resistivity, and impedance. The same method was used to fabricate samples from the other test groups. The conductivity and resistivity of each W-paste sample ($n = 5$) were measured using a 4-point probe system (Ossila, Ltd., UK) with adjusted scale factors (e.g., scale of the samples) to convert the sheet resistance to conductivity and resistivity. The average conductivities of the center, top, bottom, left, and right regions were measured for each sample to eliminate the outlier effect. The resistivities of the Sn solder, Ag paste, and Ag epoxy in Fig. 1f have been referenced in previous studies [28,40–42]. The impedance change of the W-paste and particle size were measured using a frequency response analyzer (FRA, Autolab FRA32 M, Netherlands). To evaluate the isotropic conductivity, PDMS molds filled with W- and Mo-pastes were placed in an oven at 85 °C for 24 h, and the subsequent solidification at room temperature yielded cylindrical samples. A multimeter and test probes were used to measure the resistance differences, which represent the isotropic conductivity of the W-paste. All the measurements were conducted at 25 °C.

2.3. Dissolution tests

A bioresorbable wireless stimulator was prepared using Mg foil (50 μm, Nilaco Co., Japan) ablated with an ultraviolet (UV) laser marker (MD-U1000C, Keyence, Japan), a silicon (Si) nanomembrane diode, and poly (lactide–*co*–glycolide) (PLGA) encapsulation layers [9]. The W-paste served as an interconnection for each component. The stimulator was immersed in PBS 1X and placed in an oven at 50 °C for 60 d to monitor the dissolution status. A 200 μm-thick W-paste coating was screen-printed using a polyimide (PI) stencil on a stainless-steel sheet to yield a "K"-shaped mark for monitoring the dissolution. Before measuring the section profile of the mark, a sample was retrieved from the PBS, rinsed with distilled water, and stored under vacuum for 24 h to minimize the W-paste swelling. Each group of samples (days 1 and 60) was prepared for X-ray photoelectron spectroscopy (XPS, ULVAC-PHI X-TOOL, Japan) analysis as square plates (5 mm × 5 mm × 1 mm) and immersed in PBS 1X for 1 or 60 d at 37 °C, respectively. The samples were then retrieved from the PBS, rinsed with distilled water, and stored in a drying oven at 40 °C for 24 h to remove any residual moisture. The XPS peaks were analyzed using XPSPEAK 4.1 free software.

2.4. Mechanical tests

Melted candelilla wax and beeswax were poured into 3D-printed molds (10 mm × 10 mm × 5 mm) and covered with a glass slide. The detachment of the glass slide from the solidified wax resulted in a smooth surface for the Vickers hardness tests (Duramin 4, Struers LLC, USA). The hardness test parameters were HV0.01/10 and ambient temperature (22 °C). The 3-point-bending-test samples were prepared as 35 mm × 3.2 mm × 2.5 mm (width × diameter × height, respectively), and the tests were conducted according to the standard for flexural properties of nonreinforced and reinforced plastics (ASTM D790) using a universal test machine (UTM, Cellscale, Canada). Compression test samples were fabricated using a PDMS mold, and the tests were conducted according to the standard method for testing the compressive properties of rigid plastics [American Society for Testing and Materials (ASTM standard D695)] with the UTM. The contact angles of water droplets on various W-paste samples were measured using a contact angle meter/analyzer (Phoenix 300, SEO, Korea), and the data for each sample ($n = 5$) were collected and analyzed using embedded software. Focused ion beam–scanning electron microscopy (FIB-SEM; Helios 5 UC, FEI, USA) was used to obtain energy-dispersive X-ray spectroscopy (EDS) and backscattered electron (BSE) mapping images.

2.5. Fabrication and testing of fringing-effect sensor

Poly butanedithiol 1,3,5-triallyl-1,3,5-triazine-2,4,6(1*H*,3*H*,5*H*)-trione pentenoic anhydride (PBTPA) was synthesized as encapsulation and dielectric layer according to a previously published method [43], with a molar ratio of 1:4:7, and all the chemicals were purchased from Sigma–Aldrich Co., USA. The synthesized PBTPA was stored in an amber screw vial for 2 days. The electrodes were fabricated using a Mo film (Nilaco Co., Japan). The W-paste was connected to 50 μm molybdenum wires and electrodes. Half-cured PBTPA (stored for 2 days) of 100 μm thickness was spread on a glass slide and then fully cured in a UV chamber (Korea Ace Sci., Korea) for 10 min. The cured PBTPA and fabricated electrodes were treated with plasma (ELECTRO-TECHNIC PRODUCTS, Inc., USA) and attached. Half-cured PBTPA of 100 μm thickness was spread and then fully cured by UV. As in the previous method, the second electrode and encapsulation layer were placed on the

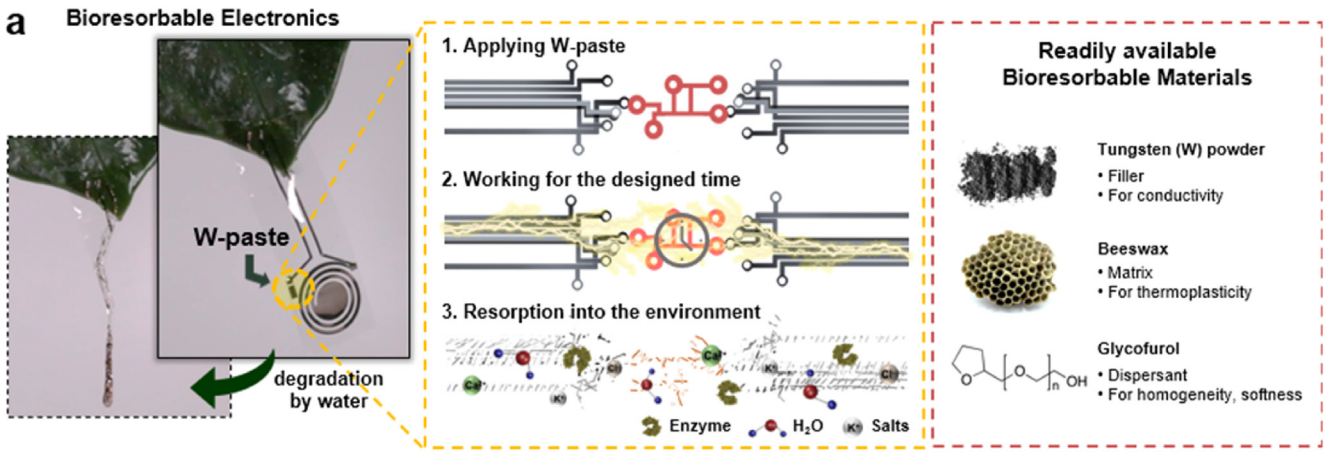

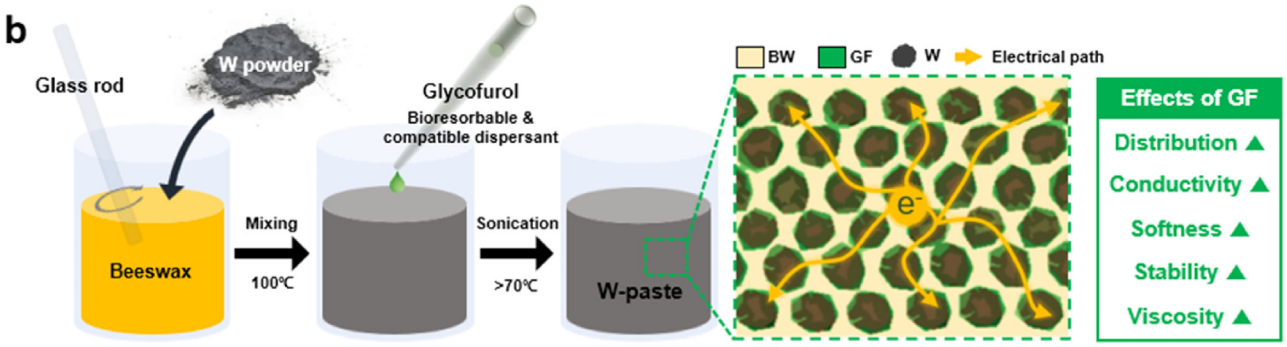

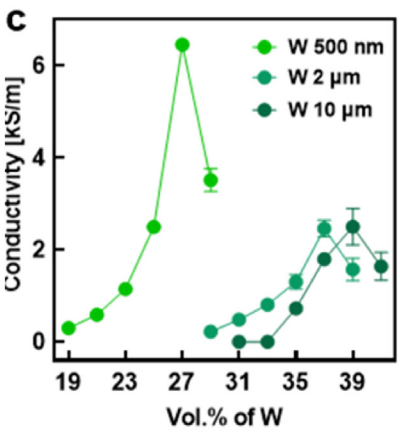

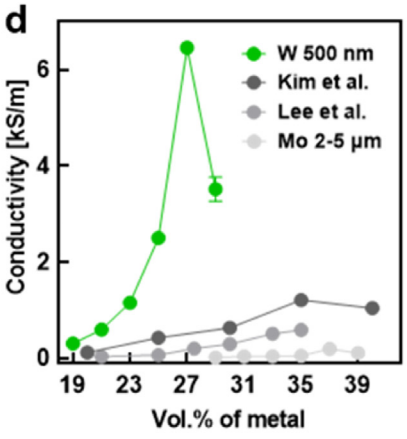

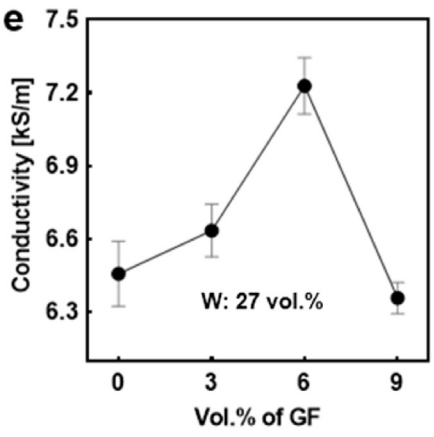

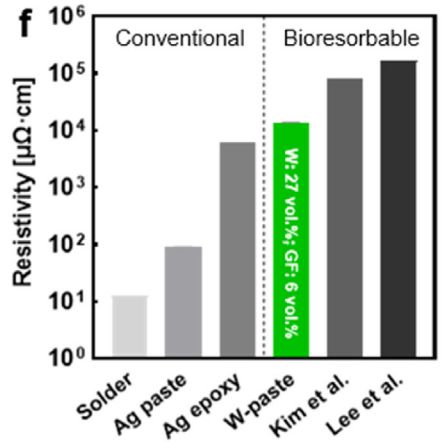

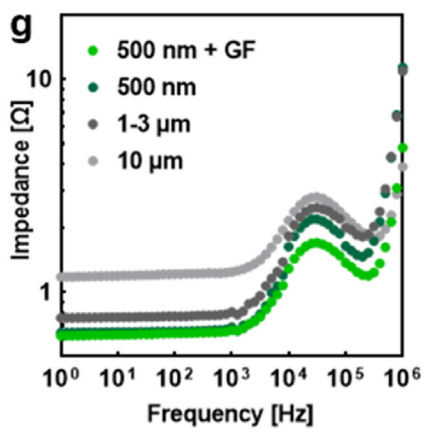

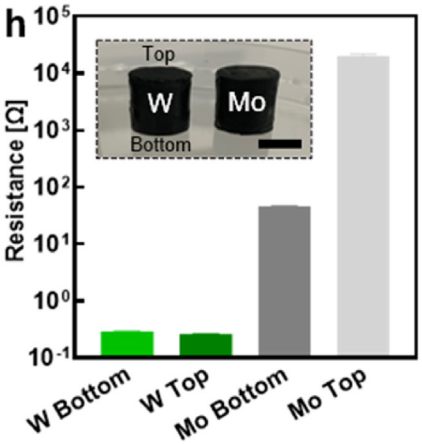

(caption on next page)

Fig. 1. Conceptual design and electrical properties of bioresorbable and conductive tungsten paste (W-paste). (a) Illustrations of lifetime-designed W-paste interconnection for application to W-paste-based bioresorbable electronics and materials **(b)** Schematic of the fabrication process of W-paste and effects of glycofurol. **(c)** Electrical conductivity measured using 4-point probe system and plotted as functions of tungsten particle volume fraction and radius (light, medium, and deep green represent 500 nm, 2 μm, and 10 μm particles, respectively). **(d)** Comparison of conductivities achieved using W-paste and bioresorbable composite pastes previously prepared using molybdenum (Mo) particles or polybutylene adipate–*co*–terephthalate (PBAT) matrix. Compared to other bioresorbable composite pastes, W-paste (light green) exhibits at least four times higher electrical conductivity. **(e)** Conductivity enhancement of W-paste by uniformly distributed GF in 27 vol% tungsten powder in beeswax matrix. **(f)** Comparison of electrical resistivities achieved using conventional Sn solder, Ag paste, and Ag epoxy adhesive and bioresorbable W-paste-based interconnection materials prepared using 27 and 6 vol% tungsten and GF, respectively. **(g)** Impedance measurements of W-pastes prepared using various sizes of W particle and GF contents. **(h)** Surface resistances of W- and Mo-paste blocks for investigating phase separation between top and bottom regions. Inset shows 8 mm-high × 6 mm-diameter blocks of metal particles/wax (left: W; right: Mo) used in this experiment. Scale bar represents 5 mm.

PBTPA film. The fringing-effect sensor was placed in a syringe and connected to the outlet of a commercial pressure sensor (MPX5700, Freescale Semiconductor, Inc., USA). An analog-to-digital converter (ADC, 7747 CE, Analog Device Inc., USA) connected to a computer was used to collect the capacitance data of the fringing-effect sensor.

2.6. In vitro live/dead assay

In vitro cytotoxicity and immune response tests were performed using C2C12, 3T3L1, and RAW 264.7 cells cultured in Dulbecco's Modified Eagle Medium (DMEM) supplemented with 10% fetal bovine serum (FBS) and 1% penicillin-streptomycin (PS). The cells were incubated at 37 °C in a humidified incubator with 5% CO_2. Eluates were obtained from the materials (beeswax, beeswax + W, and W-paste) according to the International Standards Organization (ISO) 10993-12 standard. The culture media (20 mL) containing 4 g of material were incubated at 37 °C for 72 h and subsequently stored at 4 °C until further use.

For the live/dead assay, mouse fibroblasts were cultured on 48-well plates at a density of 1.5×10^4 cells per well for 24 h. The cells were then treated with eluate obtained from each material. Seven days after the treatment, a live/dead viability/cytotoxicity kit was used to determine the cell viability. The working solution, including ethidium homodimer-1 (EthD-1) and calcein AM, was added to each well. All the processes were performed under low-light conditions. After 30 min of incubation at room temperature, the live and dead cells were observed under a fluorescence microscope (Zeiss, Germany).

2.7. In vitro WST1 cytotoxicity assay

Before the cell viability experiments, the C2C12 and 3T3L1 cells (1.0×10^4 cells per well) were cultured in 96-well plates for 24 h in an incubator with 5% CO_2 at 37 °C. The incubated cells were treated with the eluates in the 96-well plates. Seven days after the treatment, the reagent from the WST1 cytotoxicity kit was used. After incubation for 3 h, the cell viability was examined at 450 nm using a microplate reader (Synergy H1, BioTek, Vermont, USA).

2.8. In vivo biocompatibility tests

Male BALB/c mice (20–30 g) were purchased from Nara Biotech Co., Ltd. (Seoul, Korea). Avertin (anesthetic; 2.5%), IVD Black silk (11 mm, AILEE), BD Ultra-Fine Insulin Syringe [1 mL, 0.25 mm (31 G) × 8 mm], blood collection tubes [with K2E ethylenediaminetetraacetic acid (EDTA) 18.0 mg, 10.0 mL], and 4% paraformaldehyde solution (BYLABS) were used.

The biocompatibility of the W-paste was assessed in 15 BALB/c mice (male, 6 weeks old). The mice were divided into PLGA, PDMS, and W-paste groups as positive control, negative control, and test sample, respectively after a diurnal cycle for 1 week before the surgery. The mice were anesthetized using an intraperitoneal injection of 2.5% avertin.

Each sample was prepared with a size of 5 mm × 5 mm thickness of 100 μm. Prior to implantation, the test and control materials were sterilized using UV irradiation. The sterilized materials were then implanted in subcutaneous mouse tissues on the dorsal side of the animal for four weeks. The body weights of the mice in the test and control groups were measured weekly for four weeks after implantation.

2.9. Cytokine analysis

Mouse macrophages were cultured in 24-well plates at 5×10^4 cells per well for 24 h for the proinflammatory cytokine enzyme-linked immunosorbent assay (ELISA). The incubated cells were treated with eluates. Seven days after the treatment, the supernatant was collected and centrifuged to remove any cell fragments. After the centrifugation, the TNFα, IL-1β, and IL-6 protein expressions were detected using ELISA kits.

Four weeks after the implantation, mouse blood samples were collected using cardiac puncture with a BD ultrafine insulin syringe to determine the blood chemistry. Then, the mice were sacrificed by cervical dislocation, and the skin tissue surrounding the implanted materials was carefully harvested and immediately fixed using 4% paraformaldehyde. The collected tissues were blocked using paraffin embedding, sliced using a microtome, and stained with Masson's trichrome and hematoxylin and eosin (H&E) reagents. The structure of the skin tissues was analyzed using an optical microscope (OM; DM IL LED, Leica, Germany).

2.10. Hematology analysis of blood samples

Each collected blood sample ($n = 13$) was aliquoted into a K2EDTA tube (BD Vacutainer) to prevent clotting. The blood samples were sent to NEODIN BioVet, where a complete blood count (CBC) test was performed, and the numbers of white blood cells (WBCs), neutrophils, lymphocytes, and monocytes were determined for each animal.

3. Results and discussion

3.1. Material design and fabrication of bioresorbable and conductive W-paste

Conductive and bioresorbable W-paste, comprising a mixture of W nanoparticles and GF in a beeswax matrix, serves as an electrical interconnect within a predesigned lifetime. Fig. 1a shows the life sequence of the W-paste in the bioresorbable device and information about the constituent components. Once used for the intended time, the W-paste chemically dissociates and is safely resorbed by the surrounding environment of the adjacent tissue (e.g., enzymes, ions, water, and mechanical stresses). All the W-paste constituents (W, beeswax, and GF) are bioresorbable, biocompatible, and readily applicable without additional synthesis steps. Using these materials, the W-paste is fabricated quickly (within 10 min) and straightforwardly, as shown in Fig. 1b. The W particles (~500 nm) were mixed with the melted beeswax in a precisely controlled volume fraction at 100 °C, and a trace of GF (~6 vol %) was added to obtain the W-paste. W is a well-known biocompatible metal widely used in prosthetics and medical implants, and previous studies have shown that W exhibits *in vivo* bioresorption [3,44–46]. These biocompatible W particles provide electrical pathways for the W-paste through the internal electrical conduction of a single particle and tunneling effects between the metal particles [47,48]. Beeswax exhibits a thermoplastic matrix and a relatively low melting point (65 °C). Thus, the W-paste requires less time and can be safer to process than other

bioresorbable interconnections requiring high temperatures, solvent casting, and UV curing for the same applications [28,40,49]. The softness of beeswax (in the range 200–300 MPa) at room temperature results in the formation of robust interconnections in flexible electronics by reducing the mechanical mismatch between the W-paste and substrates (e.g., PI: in the range 100–200 MPa; PLGA: ~30 MPa) [50]. The GF acts as a solvent for insoluble active materials and is a biocompatible surfactant that distributes PLGA microspheres in various solvents [51,52]. In this study, the GF helps to disperse the W particles homogeneously, which enhances the softness and isotropic conductivity of the W-paste. In addition, the W-paste has shape retention ability even above the melting point and guarantees dimensional accuracy owing to the GF-induced high surface tension and viscosity.

3.2. Electrical properties of W-paste

To optimize the material mixing ratio, a four-point probe system (T2001A3, Ossila) was used to evaluate the electrical properties of various W-pastes. Volume fraction and size of W particles are the major variables affecting the electrical conductivity, which depends on following electrical percolation conductivity formula [53,54]:

$$\sigma = \sigma 0(\varphi - \varphi c)t \tag{1}$$

where σ is the electrical conductivity, φ is the volume fraction, φc is the percolation threshold, and t is the critical exponent. φc and t value of W-paste are 0.19 and 1.6, respectively (0.27,1.18 for Mo/Beeswax). The 500 nm W particles exhibited the highest conductivity (~6.4 kS/m) at a W concentration of 27 vol%. However, the 2 and 10 μm particles exhibited a relatively low conductivity (~2.9 kS/m), even at higher W concentrations of 37 and 39 vol%. According to Wu et al. [55], the interparticle distance of spherical particles in a cubic lattice can be written as

$$\delta = D\left[\left(\frac{\pi}{6\varphi}\right)^{\frac{1}{3}} - 1\right] \tag{2}$$

where δ is the interparticle distance (surface-to-surface), φ is the particle volume fraction, and D is the particle diameter. The interparticle distance becomes narrow with decreasing particle size or increasing volume fraction. Additionally, δ is related to the tunneling resistance as follows:

$$R_t = \frac{\rho_t}{\pi(\delta/2)^2} \tag{3}$$

where R_t is the tunneling resistance, and ρ_t is the inherent tunneling resistivity between the W particles. Because these equations indicate that R_t is proportional to $1/D2$, the particle size directly affects the tunneling resistance, which indicates that the 500 nm W particles exhibit higher electrical conductivity than the large particles (>1 μm) [55–57]. However, if the particle size is too small, the surface oxide layer overwhelms the entire volume, thereby shortening the intrinsic electrical pathway of the internal particles. Minimizing both the optimal particle size and volume of metal particles is critical for reducing the mechanical instability of the host material (e.g., brittleness, crazing, and shrinkage) caused by the diminishing binder coverage. For example, W-paste becomes granular when the W particles are added to the critical vol%, as shown in Fig. S1, and the electrical conductivity drastically decreases in all cases (Fig. 1c). At the optimal vol%, the W-paste exhibits four times higher electrical conductivity (~6.4 kS/m) compared to that measured in earlier studies of bioresorbable composite paste (~1.6 kS/m) (Fig. 1d) [40]. Moreover, addition of appropriate GF vol% (6 vol%) uniformly distributes the W particles in the beeswax matrix, thereby increasing the electrical conductivity by ~14% more. In contrast, as displayed in SEM images (Fig. S8c), excessive addition of GF (≥9 vol%) induces poor W distribution at W-paste surface and interrupts the electrical path of W-paste, decreasing the conductivity (Fig. 1e). Therefore, in the following experiments, 27 vol % of W particles (500 nm) and 6 vol% of GF with the beeswax matrix are considered as the optimal W-paste composition.

The low resistivity and constant impedance of the W-paste are crucial factors because high resistivity and rapid impedance changes with changing frequency adversely affect the device performance owing to the electric current fluctuations. Fig. 1f compares the resistivities of the bioresorbable interconnection materials with conventional materials (e.g., Sn solder, Ag paste, and Ag epoxy), which exhibit relatively low resistivities (11, 100, and 9.8 × 10^3 μΩ•cm, respectively). Among the bioresorbable pastes, the well-distributed W-paste achieved the lowest resistivity of up to 1.0 × 10^4 μΩ•cm, similar to that of the Ag epoxy. As shown in Fig. 1g, FRA was used to measure the impedance change of W-paste across frequencies ranging from 1 to 1.0 × 10^6 Hz. The W-paste impedance increased with increasing frequency. This result can be explained by the Drude model, which describes the electron mobility in a conductor and can be expressed as follows:

$$\mu = \frac{q\tau}{m}\frac{1}{1+\omega^2\tau^2} \tag{4}$$

where the electron mobility (μ) is a function of the frequency, ω. According to this equation, μ decreases as ω increases, and low μ causes high impedance. Impedance drop near 10^5 Hz is due to the influence of capacitance between metal particles becoming dominant in the equivalent circuit model described in Fig. S2 [58]. Additionally, the impedance increases with increasing particle size according to equations (2) and (3).

The W and Mo particles exhibit different dispersion behavior in the matrix, as empirically confirmed while preparing the experimental samples. Although the Mo particles sink when mixed with the wax, the W ones required a long time for sedimentation despite W exhibiting a higher density (19.28 g/cm^3) than Mo (10.22 g/cm^3). This may result from various factors, such as the zeta potential, steric stabilization, wettability, and surface morphology of the W and Mo particles. For example, W and Mo oxides exhibit negative and positive net charges, respectively, whereas wax esters and alcohols exhibit negative terminal functional groups (e.g., –OH and –COOH) [59,60]. This charge difference affects the double-layer repulsive and van der Waals attractive forces of each metal particle, leading to opposite dispersion conditions [61,62]. In the same context, when hardened at room temperature, the Mo paste produces a thin yellow wax layer on the top owing to phase separation, as shown in Fig. S3, whereas the W paste remains dispersed. Subsequently, W- and Mo-paste blocks of height 8 mm were prepared to investigate the phase separation between the top and bottom surfaces (Fig. 1h). The inset shows the metal particle/wax (left: W; right: Mo) blocks used in this experiment. The W-paste exhibits similar resistance between the top and bottom surfaces (0.3 and 0.5 Ω, respectively), while Mo paste exhibits an approximately two-order difference in magnitude for the bottom (~1.0 × 10^2 Ω) and top (~1.0 × 10^4 Ω) surfaces. This result confirms that the W-paste exhibits isotropic conductivity along the x-, y-, and z-axes. Moreover, SEM images ascertain that the W particles are more homogeneously suspended in the wax matrix compared to the Mo particles, which clarifies the higher electrical conductivity of W-paste (Fig. S4).

3.3. Degradation behavior and thermal characteristics of W-paste

In contrast to conventional waterproof devices, bioresorbable electronics must be dissolved by body fluids in time to secure their functionality during a predesigned lifetime. Thus, the design of each component with appropriate dissolution and stability periods is important to ensure the good functionality of the bioresorbable devices. In the same context, as the degradation progresses, bioresorbable interconnection materials should maintain electrical conductivity and act as binders for each component such as the solder in conventional electronics. Fig. 2 shows the bioresorbable features of the W-paste in various dissolution modes.

Sequential images were captured for the dissolving bioresorbable wireless stimulator immersed in PBS 1X (at 50 °C), which comprised a radio frequency (RF) power harvester and rectifying stimulation circuit interconnected by the W-paste, to provide information about accelerated degradation lifetime (Fig. 2a). All the components, e.g., the 30 μm-thick Mg RF antenna and electrode and 200 μm-thick PLGA encapsulation layer, are fully degraded in PBS at 50 °C within 60 days. In Fig. 2b, the "K"-shaped W-paste (5 mm × 5 mm × 200 μm) on the stainless-steel substrate immersed in the PBS 1X at 50 °C shows the intrinsic dissolution behavior by the section profile changes from day 1–40 and 80. Dektak XT® quantifies the W-paste sections, indicating that dissolution progresses spatially from the edge to the center, and the 200 μm-thick W-paste fully dissolves in 80 days.

XPS and SEM yielded data on the atomic-binding-energy transition and morphological changes of the W-paste surface from the early to late stages of dissolution (Fig. 2c and **d**, respectively). Fig. 2c shows the peak (35.37 eV) of the native oxide layer of the W particle (W^{6+}) and a small peak (at 41.0 eV) for the exposed W (W $5p_{3/2}$). The inset shows the SEM image of the intact surface of the W-paste. After dissolution for 60 d, the various oxide forms (W^{x+}, W^{4+}, W^{5+}, and W^{6+}: 31.25, 32.63, 33.75, and 35.72 eV, respectively) appeared with the pure W (30.25 eV), and the W $5p_{3/2}$ peak disappeared. The W particles can be reversibly oxidized and reduced to diverse states ($W \leftrightarrow WO_2 \leftrightarrow WO_{2.72} \leftrightarrow WO_{2.9} \leftrightarrow WO_3$) in the presence of H_2O [63] and finally dissolved as $W_{(s)} + 4H_2O \rightarrow WO_4^{2-}{}_{(aq)} + 8H^+ + 6e^-$ [64]. The SEM image shows surface erosion of W-paste through the roughness and pores after 60 d of degradation in PBS 1X at 37 °C. The inset of Fig. 2d and the entire degradation process are shown in Fig. S5. As shown in Fig. 2e, the conductivity changes of W-paste after 2 weeks of immersion in the PBS at 37 °C corroborates that adding a trace of GF enhances the electrical stability in a wet environment. The conductivity fluctuations in the first two days originate from the dissolution of the outer shell oxide layer of the W particles [40], whereas the electrical conductivity of samples prepared using 6% GF maintains its initial value ($C/C_0 \approx 1$) for 13 days. The conductivity of the GF-free samples deteriorates faster, and the samples lose their electrical functionality entirely at the end of the experiment. The inset shows that although no cracks formed in the GF-containing samples, the GF-free ones were severely cracked. The addition of a trace of GF also increased the mechanical strength of W-paste in subaquatic conditions.

Differential scanning calorimetry (Q 20, TA instrument) was used to determine the thermal properties of W-paste as shown in Fig. 2f. Consistent with a prior study, melting temperature is near 64 °C in the heating cycle [65]. The inset shows a detailed view of the peaks near the melting point. These results represent that W-paste upholds its functionality as an implantable material at a normal body temperature range (~37 °C) and can be processed at a relatively low temperature to minimize the damage to bioresorbable substrates or active materials.

3.4. Mechanical properties of W-paste

In previous studies, the candelilla wax used for the conductive paste matrix mainly comprised hydrocarbons (~50 wt%), especially *n*-alkanes (tritriacontane, hentriacontane, triacontane, nonacosane, and hexacosane: $C_{29–33}$) [66]. Because these long-chain hydrocarbons are crystalline at room temperature, a high hydrocarbon ratio causes brittleness when the wax is solidified [67]. Therefore, a soft beeswax matrix can be substituted for the candelilla wax because beeswax mainly comprises amorphous esters (e.g., monoesters and diesters), and the hydrocarbon ratio is comparatively low (~14 wt%) [68,69]. The Vickers hardness test (at RT: 22 °C) confirms that the beeswax is softer (0.48 HV0.01) than candelilla wax (3.65 HV0.01), as shown in Fig. 3a. The hardness of the matrix can be regulated by controlling the beeswax and candelilla wax mixing ratio. Because the hardness values are not considerably different for wax mixtures containing more than 60 wt% beeswax, a pure beeswax matrix is used to fabricate soft interconnection materials. Three-point bending tests were conducted to measure the flexural modulus variance of the W-paste block for different matrix compositions. The flexural strengths of the W-pastes prepared using the candelilla wax, beeswax, and GF-containing beeswax are 13.2, 4.9, and 3.0 MPa, and the corresponding flexural moduli are 2.64 GPa, 622 MPa, and 223 MPa. This reduced flexural modulus implies that the beeswax is more suitable than the candelilla wax for preparing the W-paste matrix and that the GF mitigates the W-paste stiffness (Fig. 3b). For the compression tests, cylindrical samples of size 7 mm diameter × 14 mm height were prepared, as shown in Fig. S6. The increasing GF content (3, 6, and 9 vol%) enhances the W-paste softness, resulting in relatively low compressive stresses (4.1, 3.9, and 3.5 MPa, respectively), while the ultimate compressive stress of the GF-free W-paste is approximately 6 MPa. An increase in the GF content reduces the compressive strength while increasing the compressive strain, as shown in Fig. 3c. The addition of 6 vol% GF enhances the W-paste compressive strain from 7 to 15%, and the optimal W particle dispersion may affect the W-paste compressive strain.

Because the proportion of beeswax in W-paste is higher than tungsten (W/beeswax = 27/73), the estimated surface wettability of the W-paste suggests that it is close to hydrophobic. However, the oxides on particle surfaces are hydrophilic (contact angle <5°) [70]. The extreme wettability difference weakened the adhesion between the beeswax and W particles [71–74]. Surfactants, such as GF can reduce the wettability difference. On the surface, the water contact angles decreased with increasing GF content (110° and 81° at 0 and 6 vol%, respectively), which indicates that the GF effectively increases the beeswax wettability (Fig. 3d). In addition, the GF in the W-paste can mitigate the matrix-shrinkage-induced internal residual stress, which overwhelms the adhesion force and induces mechanical instability. As shown in Fig. 3e, several microfractures were observed using OM, indicating that the internal stress induced a crazing effect on the GF-free W-paste surface. In contrast, W-paste containing GF did not exhibit any crack, which suggests that GF can mitigate the residual stress and increase the surface adhesion between the filler and matrix. The W-paste-coated PI film endured various deformations (e.g., bending and twisting) without delamination. The maximum bending radius is 5 mm for the 100-μm-thick film (Fig. 3f). 180° peel and lap shear tests were conducted to investigate W-paste adhesion properties at other substrates, including metal (e.g., Mg) and polymers (e.g., LDPE, PI) (Fig. S7). A BSE image confirmed microstructural improvements through the homogeneous distribution of W particles in the W-paste matrix. The W-powder agglomeration is displayed as a saturated GF-free white region (indicated by the green arrows on the left side in Fig. 3g). After GF was added, the W particles were uniformly dispersed without any aggregated regions (on the right side in Fig. 3g). The EDS maps also suggest that the W and carbon (C) particles were well distributed in the beeswax matrix. The EDS mapping images show that the yellow region (W) covers most of the GF-free matrix before adding GF and that the sky blue (C) and yellow W regions are evenly distributed in the GF-containing matrix (Fig. S8).

3.5. Applications of bioresorbable W-paste

Fig. 4 shows the various resorbable electronics applications fabricated using the W-paste. Fig. 4a shows a neat and precise screen-printed W-paste pattern exhibiting excellent conductivity and enabling the fabrication of a power-delivery antenna. UV laser ablation is used to carve the pattern and fabricate a 100 μm-thick trench for the coil on the PI tape, which is attached to a glass slide substrate. The melted W-paste at 70 °C was screen-printed to fill the trench, and the PI tape residue was removed after solidification of the W-paste at room temperature (RT). The obtained 1 mm-wide × 100 μm-thick receiver coil exhibited an 800 μm interline gap and seven turns in a 60 mm × 40 mm rectangle. The function generator transports power to the receiver coil by inductive coupling at 10 V_{p-p} and 10 MHz, and the delivery distance is 7 cm without any power amplification. A micro-LED indicates the wireless power delivered to the receiver coil. Fig. 4b shows W-paste contact pads fabricated with various line widths ranging from 200 μm to 800 μm and the same screen-printing method used for fabricating the coil, and the

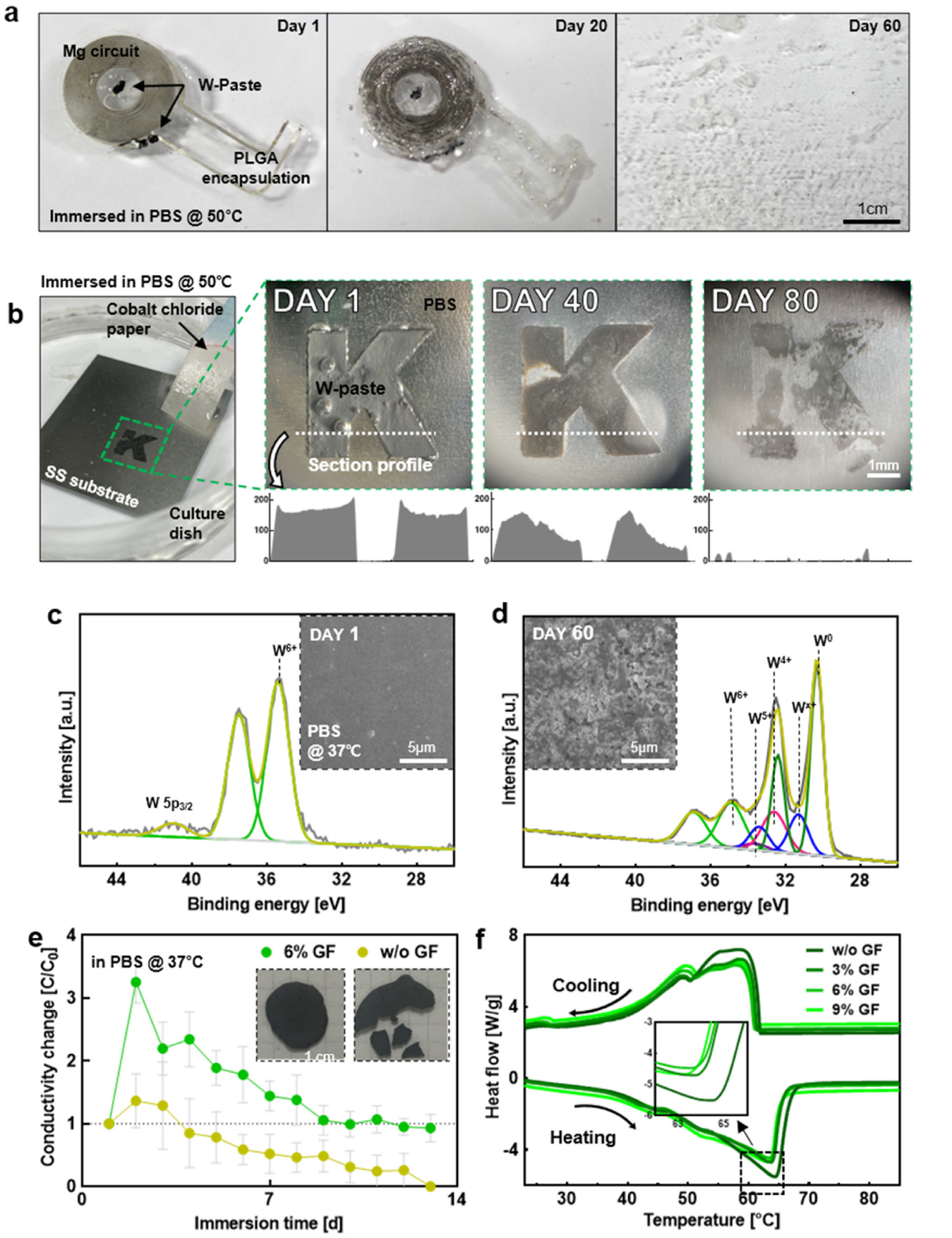

(caption on next page)

Fig. 2. Degradation behavior and thermal properties of W-paste. (a) Sequential images showing dissolution of bioresorbable wireless power-harvesting and -stimulation device connected to each part using W-paste and immersed in phosphate-buffered saline (PBS) 1X concentration at 50 °C. **(b)** "K"-shaped W-paste (5 mm × 5 mm × 200 μm) coated on stainless steel substrate to examine dissolution for different immersion times in PBS 1X at 50 °C.Images show W-paste dissolution by section profile and vanishing "K" shape. Tungsten atomic-binding-energy transition analyzed by X-ray photoelectron spectroscopy (XPS) at W-paste surface on days **(c)** 1 and **(d)** 60. Gray, light green, purple, magenta, blue, and deep green represent baseline, W^{6+}, W^{5+}, W^{4+}, W^{x+}, and W^{0}, respectively. Inset shows surface morphology changes of W-paste in scanning electron microscope (SEM) images. **(e)** W-paste conductivities measured in wet environment (PBS 1X at 37 °C) over 2 weeks. Green and yellow represent 6 vol% GF and GF-free W-pastes, respectively. Inset images show fragmented GF-free and intact GF-containing W-paste samples at the end of the test. **(f)** DSC results for W-pastes containing various GF contents in beeswax matrix. Inset shows magnified peaks inferring W-paste melting point.

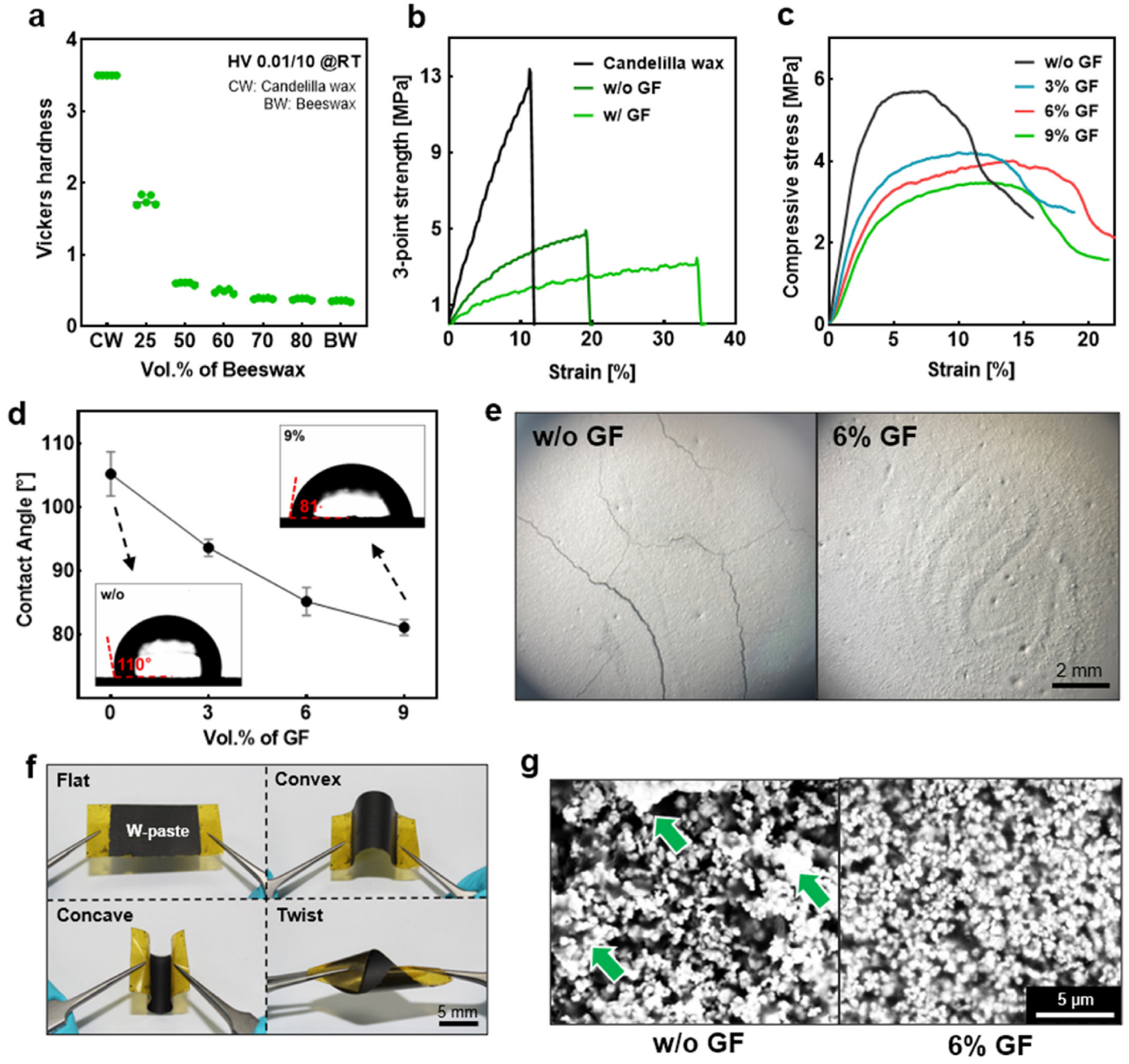

Fig. 3. Mechanical properties of W-paste. (a) Vickers hardness values measured at room temperature (RT: 22 °C) indicating that beeswax (0.48 HV0.01/10) is softer than candelilla wax (3.65 HV0.01) and their mixtures. **(b)** Flexural stress-strain curves of W-pastes prepared using various matrices. Light green, green, and black represent GF-containing and -free W-paste and candelilla wax/W matrices, respectively. **(c)** Compressive stress-strain curves of W-pastes prepared using various vol% of GF in beeswax matrix. Black, blue, red, and green represent 0, 3, 6, and 9 vol% GF, respectively. **(d)** Contact angle plotted as a function of GF vol% for W-paste surfaces. Inset presents contact angles of water droplets on surfaces of W-pastes prepared using 0 or 9 vol% GF in beeswax matrix. **(e)** Optical microscopy images showing surfaces of W-pastes prepared using different GF contents in beeswax matrix. **(f)** W-paste-coated polyimide (PI) film under convex and concave bending and twisting deformations. **(g)** SEM images of W-paste microstructure photographed in backscattered electron (BSE) mode. Green arrows indicate tungsten-particle agglomeration in GF-free beeswax matrix.

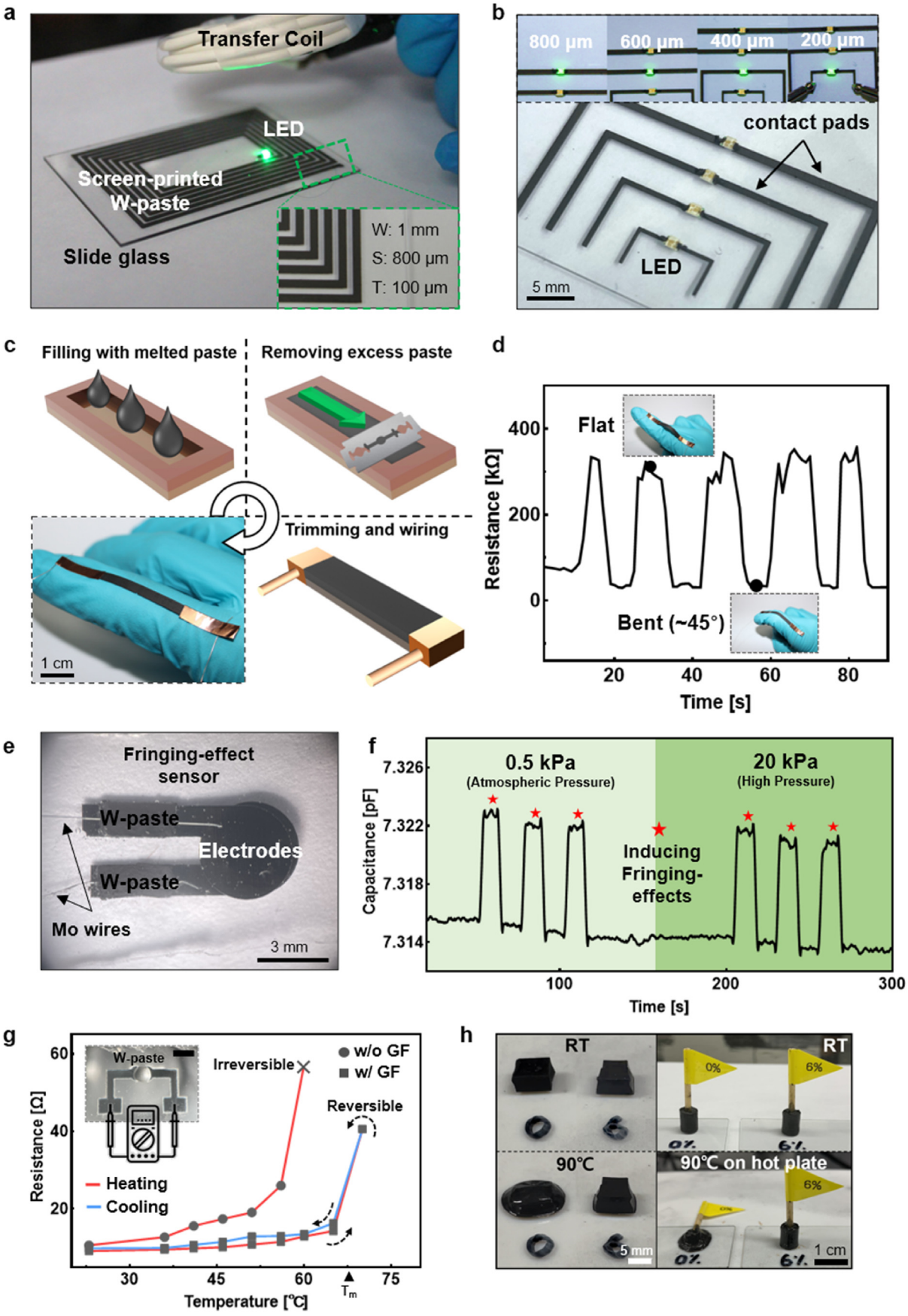

(caption on next page)

Fig. 4. Applications of W-paste in bioresorbable electronic devices. (a) Screen-printed rectangular W-paste-based antenna coil for power delivery. (Inset shows part of 60 mm × 40 mm rectangular 1 mm-wide and 100 μm-thick antenna coil exhibiting 800 μm spacing. **(b)** W-paste-based contact pads integrated with micro-LEDs on a glass slide exhibiting various line widths narrowing from top to bottom (800 and 200 μm, respectively). Inset shows that micro-LEDs light up when 1.5 V is applied to both ends of contact pad. **(c)** Schematic of W-paste-based flex sensor fabrication. **(d)** Resistance data obtained from flex sensor by repeated bending of a finger. Inset images show magnitude of bend at each data point. **(e)** Fully bioresorbable fringe-effect capacitive sensor fabricated using Mo electrodes and wires for generating electric field and transmitting data, respectively, W-paste-based interconnections, and bioresorbable polyanhydride-based encapsulation layer. **(f)** Capacitances generated for different fingertip proximities at atmospheric and high pressures. **(g)** W-paste resistances. Squares and circles represent GF- containing and -free W-pastes, respectively, under heating and cooling cycles. Inset shows experimental setup for resistance measurements (two Mo contact pads connected by W-paste). **(h)** Melting behaviors and viscosities of W-pastes prepared using different GF contents.

micro-LED between the contact pads was linked using a soldering iron. The W-paste dimensional range can be freely modified as required, and the contact-pad feasibility is maintained regardless of the line width. This underscores the W-paste applicability for bioresorbable microsystems. The dimensional accuracy of the printed W-paste was also confirmed using quality-sensitive barcode patterns (Fig. S9).

Fig. 4c shows a schematic of the flex sensor fabrication using the W-paste. The PI tape on the PI substrate served as a mold and was filled with the melted W-paste. The excess W-paste must be removed using a razor to control the flex sensor thickness. The border was trimmed, and copper tape wiring was used to complete the signal-acquisition sensor. When attached to a finger, the flex sensor can recognize bending/straightening motions by changing the resistance. The resistance increased and decreased when the finger was folded and unfolded, respectively (Fig. 4d). Although the bending motion usually raises the resistance, our flex sensor shows opposite behavior, which may be related to Poisson's ratio of the W-paste layer in the flex sensor. The bending-induced horizontal strain generates vertical compression, thereby decreasing the distance between particles and the tunneling resistance owing to closer W particles (Fig. S10). The fully bioresorbable fringe-effect capacitive sensor shown in Fig. 4e demonstrates the functionality of a W-paste interconnection. Fringe-effect capacitive sensors identify the approaching object by the capacitance change when the object interrupts the fringe field near the sensor, which is encapsulated in a bioresorbable polyanhydride layer and comprises Mo electrodes and wires (to generate an electric field and transmit data, respectively) and W-paste interconnections. The sensor size is approximately 3 mm (W) × 5 mm (L) × 1 mm (H). In a 10 mL syringe, the sensor detected fingertip-movement-induced capacitance changes. At both standard (atmospheric) and high hydrostatic (121 kPa) pressures regulated by the syringe plunger, the W-paste interconnections provided stable noise-free signals from the sensor despite the small capacitance change (~0.1 pF). In addition, the difference between the signal amplitudes was negligible in both states (Fig. 4f).

The GF provides resistance recovering ability to the W-paste during the heating and cooling cycles. A simple open circuit interconnecting two adjacent contact pads (e.g., a 15 μm-thick Mo film) on a PDMS (Sylgard™ 184, Corning) substrate with W-paste served as a contact site for measuring the W-paste resistance change at different temperatures. Although the resistance of the heated GF-containing W-paste returned to its original value as the W-paste cooled, the GF-free W-paste permanently lost its electrical conductivity when the temperature exceeded the melting point. Larger square W-paste blocks were placed on a hot plate to verify their temperature resistance (Fig. 4g).

Interestingly, W-paste without GF melted like pure wax, while W-paste with GF maintained the original shape above the melting temperature (90 °C), as shown in **Supplementary Video 1**. Similar to the W-paste prepared using the sol-gel process, W-paste prepared using GF exhibits high viscosity without any physical crosslinking, and the high-viscosity W-paste can support the weight of a flag comprising a skewer stuck in the W-paste (Fig. 4h).

3.6. Biocompatibility of bioresorbable W-paste

Biocompatibility is crucial for using the W-paste as a constituent material for implantable and bioresorbable electronics.

Fig. 5 summarizes the results of the *in vitro* biocompatibility tests used to determine the W-paste latent risk. The fluorescence images of the live/dead assay for the mouse fibroblasts were used to compare the cytotoxicity of the control and test groups, as shown in Fig. 5a. In the test groups, the beeswax, beeswax + W, and W-paste eluates were used according to the ISO 10993-12 standard for evaluating the biocompatibility of medical devices to manage biological risk [75–77]. The proportion of living cells in all the test groups over seven days was the same as in the control group. These results indicate that the W-paste cytotoxicity was negligible, similar to that of the control.

Additionally, a cell viability WST1 assay (EZ cytox, Dongenbio) was conducted to determine the biocompatibility of the material. The 3T3L1 fibroblasts and C2C12 myoblasts were selected because they are the most prominent cells in the connective and muscle tissues, having direct contact with the subcutaneously implanted materials [78–80]. The 3T3L1 and C2C12 cells were treated with beeswax, beeswax + W, and W-paste eluates for 7 d; then, each cell viability was compared using the WST1 assay (Fig. 5b). The mouse fibroblast viability remained over 90% in the beeswax, W + beeswax, and W-paste groups compared with that of the control. Additionally, the mouse myoblast viability was approximately 80% in the beeswax, beeswax + W, and W-paste groups. Overall, the biocompatibility of the *in-vitro* model suggests that the W-paste is an appropriate candidate material for application to bioelectronic devices owing to its nontoxicity.

To evaluate the *in vivo* biocompatibility, identically sized PLGA, PDMS, and W-paste patches were implanted in the subcutaneous space of healthy BALB/c mice as positive controls, negative controls, and test material, respectively. Four weeks after the implantation, the blood and tissue analyses verified the immune responses in the mice, and the measured weight of the mice represented their overall health status. As shown in Fig. 6a, there were no significant differences in the weight changes between the groups. The morphology of the tissue in contact with the implanted materials was not deformed in the W-paste group compared to that of the tissue in the control group (Fig. S11a). The Masson-stained images in Fig. 6b show the formation of fibrotic tissues in each group. The fibrotic tissue thickness was measured between the area of contact with the material and the adjacent muscle tissue, and the PDMS group exhibited the thickest fibrotic tissue. Importantly, the W-paste group exhibited the thinnest fibrotic tissue (e.g., the PLGA, PDMS, and W-paste groups exhibited 0.37-, 0.794-, and 0.217-mm-thick fibrotic tissues, respectively. The scale bar represents 0.5 mm).

In the human body, fibrosis is highly correlated with inflammation. According to previous studies, beeswax exhibits inherent bactericidal properties and reduces the immune response [81–83]. Furthermore, W reportedly does not boost immune factors unless excess W accumulates [84,85]. LD50 value for dermal acute toxicity of W is 2000 mg/kg [86]. Given that the total amount of W does not exceed 1 mg in actual application, it is safe for the host to use W-paste as implantable material. To verify the immune suppression effect of the material, we cultured mouse macrophage cells (RAW 264.7) with W-paste and detected the TNF-α, IL-6, and IL-1β proinflammatory cytokines using ELISA kits. The W-paste group cells treated for 7 d with the material exhibited 3-, 2.5-, and 1.3-fold decrease in TNF-α, IL-6, and IL-1β inflammatory cytokine expressions than the control group cells, suggesting that the W-paste group induces a low inflammatory response from macrophages, thereby inhibiting the material-induced fibrosis formation in the body (Fig. 6d–f). Regarding *in vivo* bioresorption, W and its oxides dissolve as soluble WO_4^{2-} ion in

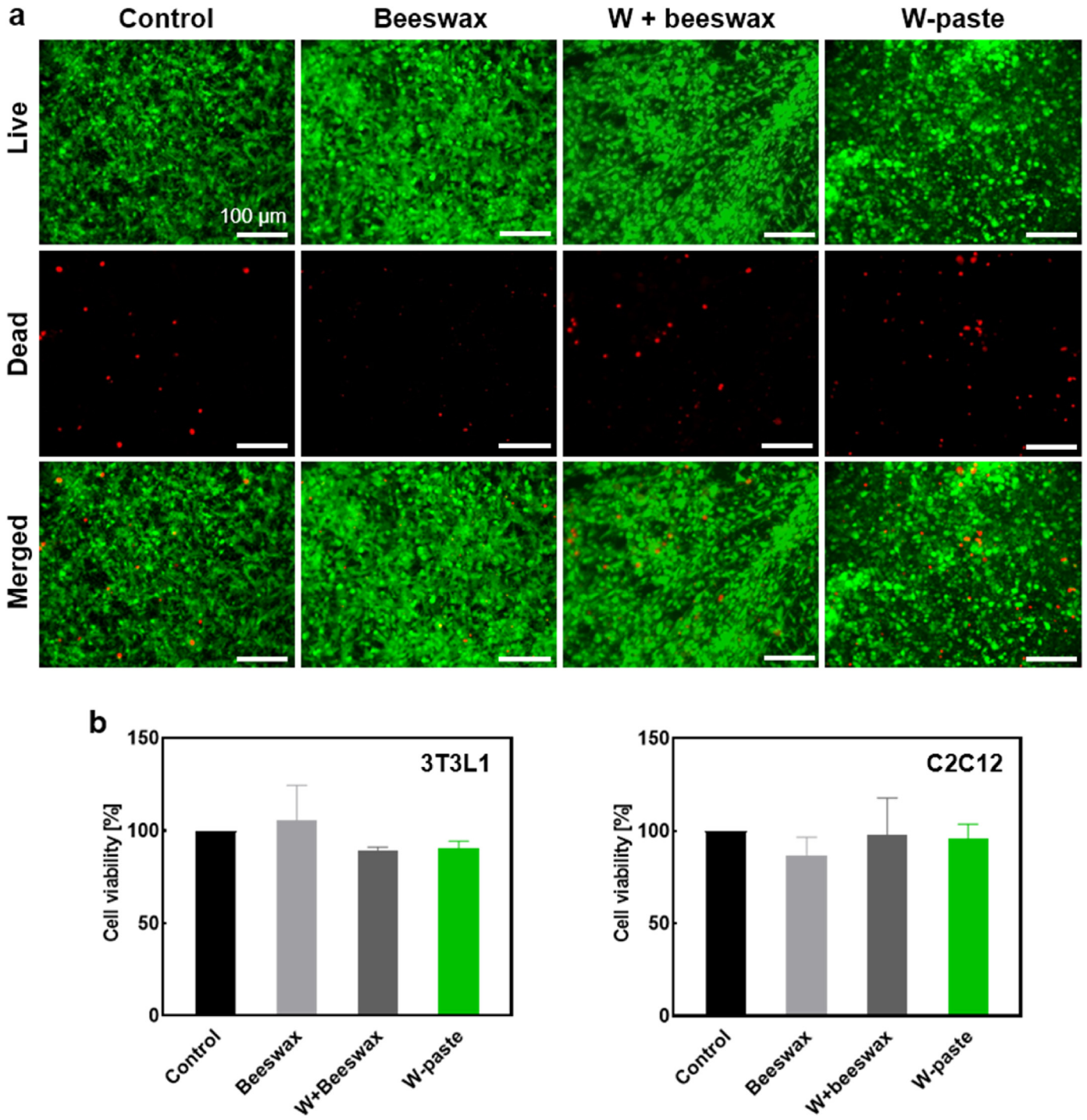

Fig. 5. Cytotoxicity of bioresorbable W-paste materials. (a) Fluorescence images of live/dead (represented by green/red, respectively) and merged assays for mouse fibroblasts in beeswax, W + beeswax, and W-paste eluates. Scale bars represent 100 μm. **(b)** Data obtained from 7 days of cell viability testing using WST1 assay with 3T3L1 fibroblasts and C2C12 myoblasts. Data are represented as mean ± standard error of mean (SEM).

biofluids, and then, they are excreted by the urinary system [87]. Prior ICP-MS studies tracking W *in vivo* presented that after acute exposure to water containing W, the W level of each organ turnarounds within 72 h [88–90].

4. Conclusions

The developed composite comprising beeswax, W particles, and GF serves as a bioresorbable interconnection material that is highly conductive and mechanically stable. Characterization by a series of experiments set the criteria for optimal material design and provided information about the electrical, mechanical, and degradation properties. The *in vitro* and *in vivo* biocompatibility tests both showed the safety of the W-paste as an implantable material. The introduction of the thermoplastic beeswax as a base material made W-paste applicable to heat streams and robust to mechanical stress compared with other materials. The GF-induced viscosity provides usability and dimensional accuracy to this material when applied as an interconnection and further provides an isotropic

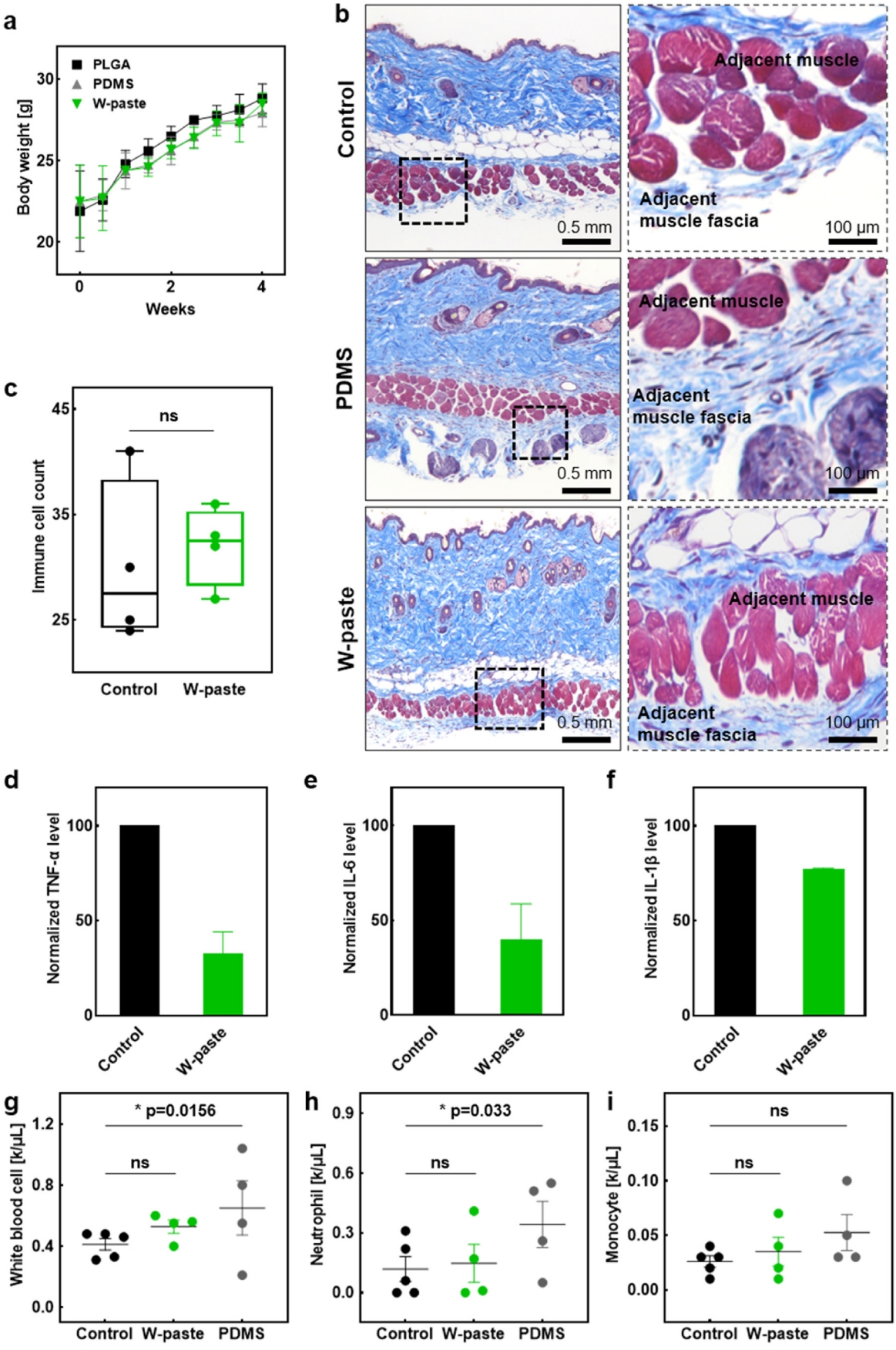

(caption on next page)

Fig. 6. Immune responses of W-paste constituent materials. (a) Weekly body weight changes of mice in PLGA (positive) and PDMS (negative) control and W-paste test groups represented by black, gray, and green, respectively. Error bars were obtained based on five independent weight measurements ($n = 5$). **(b)** Representative images of skin sections stained using Masson's trichrome reagent 4 weeks after materials were implanted in mice in PLGA, PDMS, and W-paste groups. **(c)** Average numbers of immune cells calculated for control and wax groups by counting cells in four selected areas of H&E-stained tissue images. **(d)–(f)** ELISA analyses of TNF-α, IL-6, and IL-1β proinflammatory cytokine concentrations in eluate-induced mouse macrophages in beeswax, beeswax + W, and W-paste groups. **(g)–(i)** Graphs for (d) white blood cell, (e) neutrophil, and (f) monocyte counts in complete blood counts of mice implanted with control, wax, or PDMS ($n = 5$, 4, or 4, respectively); unpaired *t*-test; $^*p < 0.05$, n. s. Means "not significant.".

electrical pathway that can be utilized for the nonplanar connection of the components. Therefore, this composite material solves the problems of the previously developed bioresorbable conductive pastes, and the W-paste can be applied to bioresorbable electronic devices to enhance their performance, reliability, and stability. In addition, the W-paste can be utilized in not only biomedical but also eco-friendly products to decrease the amount of electronic waste.

Credit author statement

Kyung Su Kim: Conceptualization, Data curation, Formal analysis, Investigation, Methodology, Visualization, Writing – original draft. Woo Youl Maeng: Conceptualization, Data curation, Investigation, Methodology, Validation, Writing – review & editing, Seongchan Kim: Data curation, Formal analysis, Investigation, Methodology, Writing – original draft, Gyubok Lee: Data curation, Formal analysis, Investigation, Resources, Writing – original draft, Minki Hong: Data curation, Investigation, Writing – original draft, Ga-been Kim: Investigation, Visualization, Jaewon Kim: Investigation, Visualization, Sungeun Kim: Conceptualization, Methodology, Seunghun Han: Methodology, Jaeyoung Yoo: Methodology, Hyojin Lee: Project administration, Resources, Validation, Kangwon Lee: Project administration, Resources, Validation, Jahyun Koo: Conceptualization, Funding acquisition, Methodology, Project administration, Resources, Supervision, Writing – review & editing.

Declaration of competing interest

The authors declare that they have no known competing financial interests or personal relationships that could have appeared to influence the work reported in this paper.

Data availability

Data will be made available on request.

Acknowledgements

H.L. acknowledges the support from the Korea government (MSIT) (No. NRF-2021R1C1C1005050). K.L. granted by the Korea Health Technology R&D Project through the Korea Health Industry Development Institute (KHIDI), funded by the Ministry of Health & Welfare, Republic of Korea (grant number: HI22C1394). J.K. acknowledges the support from the Korea government (MSIT) (Grant No. NRF-2021R1A2C2094799), Korea Health Industry Development Institute (KHIDI) (Grant No. HI22C0647), and Korea University (Grant No. K2109981). This work was in part supported by the Research Institute for Convergence Science.

Appendix A. Supplementary data

Supplementary data to this article can be found online at https://doi.org/10.1016/j.mtbio.2023.100541.

References

[1] S.K. Kang, G. Park, K. Kim, S.W. Hwang, H. Cheng, J. Shin, S. Chung, M. Kim, L. Yin, J.C. Lee, K.M. Lee, J.A. Rogers, Dissolution chemistry and biocompatibility of silicon- and germanium-based semiconductors for transient electronics, ACS Appl. Mater. Interfaces 7 (2015) 9297–9305, https://doi.org/10.1021/acsami.5b02526.

[2] D. Lu, T.L. Liu, J.K. Chang, D. Peng, Y. Zhang, J. Shin, T. Hang, W. Bai, Q. Yang, J.A. Rogers, Transient light-emitting diodes constructed from semiconductors and transparent conductors that biodegrade under physiological conditions, Adv. Mater. 31 (2019), 1902739, https://doi.org/10.1002/adma.201902739.

[3] L. Yin, H. Cheng, S. Mao, R. Haasch, Y. Liu, X. Xie, S.W. Hwang, H. Jain, S.K. Kang, Y. Su, R. Li, Y. Huang, J.A. Rogers, Dissolvable metals for transient electronics, Adv. Funct. Mater. 24 (2014) 645–658, https://doi.org/10.1002/adfm.201301847.

[4] H. Acar, S. Çinar, M. Thunga, M.R. Kessler, N. Hashemi, R. Montazami, Study of physically transient insulating materials as a potential platform for transient electronics and bioelectronics, Adv. Funct. Mater. 24 (2014) 4135–4143, https://doi.org/10.1002/adfm.201304186.

[5] S.W. Hwang, H. Tao, D.H. Kim, H. Cheng, J.K. Song, E. Rill, M.A. Brenckle, B. Panilaitis, S.M. Won, Y.S. Kim, Y.M. Song, K.J. Yu, A.A. Ameen, R. Li, Y. Su, M. Yang, D.L. Kaplan, M.R. Zakin, M.J. Slepian, Y. Huang, F.G. Omenetto, J.A. Rogers, A physically transient form of silicon electronics, Science 337 (1979) 1640–1644, https://doi.org/10.1126/science.1226325, 2012.

[6] X. Huang, Y. Liu, S.W. Hwang, S.K. Kang, D. Patnaik, J.F. Cortes, J.A. Rogers, Biodegradable materials for multilayer transient printed circuit boards, Adv. Mater. (2014), https://doi.org/10.1002/adma.201403164.

[7] G. Lee, S.K. Kang, S.M. Won, P. Gutruf, Y.R. Jeong, J. Koo, S.S. Lee, J.A. Rogers, J.S. Ha, Fully biodegradable microsupercapacitor for power storage in transient electronics, Adv. Energy Mater. (2017), https://doi.org/10.1002/aenm.201700157.

[8] S.W. Hwang, S.K. Kang, X. Huang, M.A. Brenckle, F.G. Omenetto, J.A. Rogers, Materials for programmed, functional transformation in transient electronic systems, Adv. Mater. (2015), https://doi.org/10.1002/adma.201403051.

[9] J. Koo, M.R. MacEwan, S.-K. Kang, S.M. Won, M. Stephen, P. Gamble, Z. Xie, Y. Yan, Y.-Y. Chen, J. Shin, N. Birenbaum, S. Chung, S.B. Kim, J. Khalifeh, D.V. Harburg, K. Bean, M. Paskett, J. Kim, Z.S. Zohny, S.M. Lee, R. Zhang, K. Luo, B. Ji, A. Banks, H.M. Lee, Y. Huang, W.Z. Ray, J.A. Rogers, Wireless bioresorbable electronic system enables sustained nonpharmacological neuroregenerative therapy, Nat. Med. 24 (2018) 1830–1836, https://doi.org/10.1038/s41591-018-0196-2.

[10] C. Dagdeviren, S.W. Hwang, Y. Su, S. Kim, H. Cheng, O. Gur, R. Haney, F.G. Omenetto, Y. Huang, J.A. Rogers, Transient, biocompatible electronics and energy harvesters based on ZnO, Small (2013), https://doi.org/10.1002/smll.201300146.

[11] Q. Guo, J. Koo, Z. Xie, R. Avila, X. Yu, X. Ning, H. Zhang, X. Liang, S.B. Kim, Y. Yan, M.R. MacEwan, H.M. Lee, A. Song, Z. Di, Y. Huang, Y. Mei, J.A. Rogers, A bioresorbable magnetically coupled system for low-frequency wireless power transfer, Adv. Funct. Mater. 29 (2019), 1905451, https://doi.org/10.1002/ADFM.201905451.

[12] J. Koo, S.B. Kim, Y.S. Choi, Z. Xie, A.J. Bandodkar, J. Khalifeh, Y. Yan, H. Kim, M.K. Pezhouh, K. Doty, G. Lee, Y.Y. Chen, S.M. Lee, D. D'Andrea, K. Jung, K.H. Lee, K. Li, S. Jo, H. Wang, J.H. Kim, J. Kim, S.G. Choi, W.J. Jang, Y.S. Oh, I. Park, S.S. Kwak, J.H. Park, D. Hong, X. Feng, C.H. Lee, A. Banks, C. Leal, H.M. Lee, Y. Huang, C.K. Franz, W.Z. Ray, M. MacEwan, S.K. Kang, J.A. Rogers, Wirelessly controlled, bioresorbable drug delivery device with active valves that exploit electrochemically triggered crevice corrosion, Sci. Adv. 6 (2020), https://doi.org/10.1126/sciadv.abb1093.

[13] S.K. Kang, R.K.J. Murphy, S.W. Hwang, S.M. Lee, D.v. Harburg, N.A. Krueger, J. Shin, P. Gamble, H. Cheng, S. Yu, Z. Liu, J.G. McCall, M. Stephen, H. Ying, J. Kim, G. Park, R.C. Webb, C.H. Lee, S. Chung, D.S. Wie, A.D. Gujar, B. Vemulapalli, A.H. Kim, K.M. Lee, J. Cheng, Y. Huang, S.H. Lee, P.v. Braun, W.Z. Ray, J.A. Rogers, Bioresorbable silicon electronic sensors for the brain, Nature 530 (2016) 7588, https://doi.org/10.1038/nature16492, 530 (2016) 71–76.

[14] C.M. Boutry, L. Beker, Y. Kaizawa, C. Vassos, H. Tran, A.C. Hinckley, R. Pfattner, S. Niu, J. Li, J. Claverie, Z. Wang, J. Chang, P.M. Fox, Z. Bao, Biodegradable and flexible arterial-pulse sensor for the wireless monitoring of blood flow, Nat Biomed Eng 3 (2019) 47–57, https://doi.org/10.1038/s41551-018-0336-5.

[15] Y.S. Choi, Y.Y. Hsueh, J. Koo, Q. Yang, R. Avila, B. Hu, Z. Xie, G. Lee, Z. Ning, C. Liu, Y. Xu, Y.J. Lee, W. Zhao, J. Fang, Y. Deng, S.M. Lee, A. Vázquez-Guardado, I. Stepien, Y. Yan, J.W. Song, C. Haney, Y.S. Oh, W. Liu, H.J. Yun, A. Banks, M.R. MacEwan, G.A. Ameer, W.Z. Ray, Y. Huang, T. Xie, C.K. Franz, S. Li, J.A. Rogers, Stretchable, dynamic covalent polymers for soft, long-lived bioresorbable electronic stimulators designed to facilitate neuromuscular regeneration, Nat. Commun. 11 (2020) 1–14, https://doi.org/10.1038/s41467-020-19660-6.

[16] J. Lee, H.R. Cho, G.D. Cha, H. Seo, S. Lee, C.K. Park, J.W. Kim, S. Qiao, L. Wang, D. Kang, T. Kang, T. Ichikawa, J. Kim, H. Lee, W. Lee, S. Kim, S.T. Lee, N. Lu, T. Hyeon, S.H. Choi, D.H. Kim, Flexible, sticky, and biodegradable wireless device for drug delivery to brain tumors, Nat. Commun. 10 (2019) 1, https://doi.org/10.1038/s41467-019-13198-y, 10 (2019) 1–9.

[17] J. Shin, Z. Liu, W. Bai, Y. Liu, Y. Yan, Y. Xue, I. Kandela, M. Pezhouh, M.R. MacEwan, Y. Huang, W.Z. Ray, W. Zhou, J.A. Rogers, Bioresorbable optical sensor systems for monitoring of intracranial pressure and temperature, Sci. Adv. 5 (2019), https://doi.org/10.1126/sciadv.aaw1899.

[18] Q. Yang, S. Lee, Y. Xue, Y. Yan, T.L. Liu, S.K. Kang, Y.J. Lee, S.H. Lee, M.H. Seo, D. Lu, J. Koo, M.R. MacEwan, R.T. Yin, W.Z. Ray, Y. Huang, J.A. Rogers, Materials, mechanics designs, and bioresorbable multisensor platforms for pressure monitoring in the intracranial space, Adv. Funct. Mater. 30 (2020), https://doi.org/10.1002/adfm.201910718.

[19] A.A. Kazemzadeh Farizhandi, S.Z. Khalajabadi, V. Krishnadoss, I. Noshadi, Synthesized biocompatible and conductive ink for 3D printing of flexible electronics, J. Mech. Behav. Biomed. Mater. 110 (2020), 103960, https://doi.org/10.1016/J.JMBBM.2020.103960.

[20] M. Li, Y. Guo, Y. Wei, A.G. MacDiarmid, P.I. Lelkes, Electrospinning polyaniline-contained gelatin nanofibers for tissue engineering applications, Biomaterials 27 (2006) 2705–2715, https://doi.org/10.1016/J.BIOMATERIALS.2005.11.037.

[21] G. Shi, M. Rouabhia, Z. Wang, L.H. Dao, Z. Zhang, A novel electrically conductive and biodegradable composite made of polypyrrole nanoparticles and polylactide, Biomaterials 25 (2004) 2477–2488, https://doi.org/10.1016/J.BIOMATERIALS.2003.09.032.

[22] S. Wang, S. Guan, J. Wang, H. Liu, T. Liu, X. Ma, Z. Cui, Fabrication and characterization of conductive poly (3,4-ethylenedioxythiophene) doped with hyaluronic acid/poly (l-lactic acid) composite film for biomedical application, J. Biosci. Bioeng. 123 (2017) 116–125, https://doi.org/10.1016/J.JBIOSC.2016.07.010.

[23] M. Pietsch, S. Schlisske, M. Held, N. Strobel, A. Wieczorek, G. Hernandez-Sosa, Biodegradable inkjet-printed electrochromic display for sustainable short-lifecycle electronics, J Mater Chem C Mater 8 (2020) 16716–16724, https://doi.org/10.1039/D0TC04627B.

[24] D.J. Colvin, E.J. Schneller, K.O. Davis, Impact of interconnection failure on photovoltaic module performance, Prog. Photovoltaics Res. Appl. 29 (2021) 524–532, https://doi.org/10.1002/PIP.3401.

[25] R. Ramesham, R. Ghaffarian, Challenges in interconnection and packaging of microelectromechanical systems (MEMS), Proceedings. 50th Electronic Components and Technology Conference (Cat. No.00CH37070 (2000) 666–675, https://doi.org/10.1109/ECTC.2000.853230, 2000.

[26] R.K. Pal, A.A. Farghaly, C. Wang, M.M. Collinson, S.C. Kundu, V.K. Yadavalli, Conducting polymer-silk biocomposites for flexible and biodegradable electrochemical sensors, Biosens. Bioelectron. 81 (2016) 294–302, https://doi.org/10.1016/J.BIOS.2016.03.010.

[27] X. Huang, Y. Liu, S.W. Hwang, S.K. Kang, D. Patnaik, J.F. Cortes, J.A. Rogers, Biodegradable materials for multilayer transient printed circuit boards, Adv. Mater. 26 (2014) 7371–7377, https://doi.org/10.1002/ADMA.201403164.

[28] S. Lee, J. Koo, S.K. Kang, G. Park, Y.J. Lee, Y.Y. Chen, S.A. Lim, K.M. Lee, J.A. Rogers, Metal microparticle – polymer composites as printable, bio/ecoresorbable conductive inks, Mater. Today 21 (2018) 207–215, https://doi.org/10.1016/j.mattod.2017.12.005.

[29] S.M. Won, J. Koo, K.E. Crawford, A.D. Mickle, Y. Xue, S. Min, L.A. McIlvried, Y. Yan, S.B. Kim, S.M. Lee, B.H. Kim, H. Jang, M.R. MacEwan, Y. Huang, R.W. Gereau, J.A. Rogers, Natural wax for transient electronics, Adv. Funct. Mater. (2018), https://doi.org/10.1002/adfm.201801819.

[30] S. Feng, Z. Tian, J. Wang, S. Cao, D. Kong, Laser sintering of Zn microparticles and its application in printable biodegradable electronics, Adv Electron Mater 5 (2019), 1800693, https://doi.org/10.1002/AELM.201800693.

[31] Y.J. Liu, W.T. Cao, M.G. Ma, P. Wan, Ultrasensitive wearable soft strain sensors of conductive, self-healing, and elastic hydrogels with synergistic "soft and hard" hybrid networks, ACS Appl. Mater. Interfaces 9 (2017) 25559–25570, 10.1021/acsami.7b07639.

[32] Y.K. Lee, J. Kim, Y. Kim, J.W. Kwak, Y. Yoon, J.A. Rogers, Room temperature electrochemical sintering of Zn microparticles and its use in printable conducting inks for bioresorbable electronics, Adv. Mater. 29 (2017), https://doi.org/10.1002/adma.201702665.

[33] J.Y. Bae, E.J. Gwak, G.S. Hwang, H.W. Hwang, D.J. Lee, J.S. Lee, Y.C. Joo, J.Y. Sun, S.H. Jun, M.R. Ok, J.Y. Kim, S.K. Kang, Biodegradable metallic glass for stretchable transient electronics, Adv. Sci. 8 (2021), https://doi.org/10.1002/advs.202004029.

[34] W. Shou, B.K. Mahajan, B. Ludwig, X. Yu, J. Staggs, X. Huang, H. Pan, Low-cost manufacturing of bioresorbable conductors by evaporation–condensation-mediated laser printing and sintering of Zn nanoparticles, Adv. Mater. 29 (2017), https://doi.org/10.1002/adma.201700172.

[35] S. Feng, S. Cao, Z. Tian, H. Zhu, D. Kong, Maskless patterning of biodegradable conductors by selective laser sintering of microparticle inks and its application in flexible transient electronics, ACS Appl. Mater. Interfaces 11 (2019) 45844–45852, https://doi.org/10.1021/acsami.9b14431.

[36] E.J. Curry, K. Ke, M.T. Chorsi, K.S. Wrobel, A.N. Miller, A. Patel, I. Kim, J. Feng, L. Yue, Q. Wu, C.L. Kuo, K.W.H. Lo, C.T. Laurencin, H. Ilies, P.K. Purohit, T.D. Nguyen, Biodegradable piezoelectric force sensor, Proc. Natl. Acad. Sci. U. S. A. 115 (2018) 909–914, https://doi.org/10.1073/pnas.1710874115.

[37] M. Atreya, K. Dikshit, G. Marinick, J. Nielson, C. Bruns, G.L. Whiting, Poly(lactic acid)-based ink for biodegradable printed electronics with conductivity enhanced through solvent aging, Cite This: ACS Appl. Mater. Interfaces 12 (2020), https://doi.org/10.1021/acsami.0c05196.

[38] Y. Lin, Y. Hao, J. Lu, S. Choe, M. Jun Kim, T. Lim, C. Electroplated Layers Je-Yi Wu, H. Lee, C.-H. Wu, M. Abdulrhman, A. Zhakeyev, C.M. Fernández-Posada, F.P. W Melchels, J. Marques-Hueso, Routes towards manufacturing biodegradable electronics with polycaprolactone (PCL) via direct light writing and electroless plating, al -, Flexible and Printed Electronics 7 (2022), 025006, https://doi.org/10.1088/2058-8585/AC6B6E.

[39] H.A. Aziz, Comparison between field research and controlled laboratory research, Arch Clin Biomed Res 1 (2017) 101–104, https://doi.org/10.26502/acbr.50170011.

[40] K.S. Kim, J. Yoo, J.S. Shim, Y.I. Ryu, S. Choi, J.Y. Lee, H.M. Lee, J. Koo, S.K. Kang, Biodegradable molybdenum/polybutylene adipate terephthalate conductive paste for flexible and stretchable transient electronics, Adv Mater Technol (2021) 1–12, https://doi.org/10.1002/admt.202001297, 2001297.

[41] E. Çadirli, U. Böyük, H. Kaya, N. Maraşli, S. Aksöz, Y. Ocak, Dependence of electrical resistivity on temperature and Sn content in Pb-Sn solders, J. Electron. Mater. 40 (2010) 2, https://doi.org/10.1007/S11664-010-1425-8, 40 (2010) 195–200.

[42] X. Liu, S. Wu, B. Chen, Y. Ma, Y. Huang, S. Tang, W. Liu, Tuning the electrical resistivity of conductive silver paste prepared by blending multi-morphologies and micro-nanometers silver powder, J. Mater. Sci. Mater. Electron. 32 (2021) 13777–13786, https://doi.org/10.1007/s10854-021-05954-y.

[43] Y.S. Choi, J. Koo, Y.J. Lee, G. Lee, R. Avila, H. Ying, J. Reeder, L. Hambitzer, K. Im, J. Kim, K.M. Lee, J. Cheng, Y. Huang, S.K. Kang, J.A. Rogers, Biodegradable polyanhydrides as encapsulation layers for transient electronics, Adv. Funct. Mater. 30 (2020), https://doi.org/10.1002/adfm.202000941.

[44] A. Shah Idil, N. Donaldson, The use of tungsten as a chronically implanted material, J. Neural. Eng. 15 (2018), 021006, https://doi.org/10.1088/1741-2552/AAA502.

[45] M. Peuster, C. Fink, P. Wohlsein, M. Bruegmann, A. Günther, V. Kaese, M. Niemeyer, H. Haferkamp, C.v. Schnakenburg, Degradation of tungsten coils implanted into the subclavian artery of New Zealand white rabbits is not associated with local or systemic toxicity, Biomaterials 24 (2003) 393–399, https://doi.org/10.1016/S0142-9612(02)00352-6.

[46] C. Kampmann, R. Brzezinska, M. Abidini, A. Wenzel, C.F. Wippermann, P. Hebermehl, M. Knuf, R. Schumacher, Biodegradation of tungsten embolisation coils used in children, Pediatr. Radiol. 32 (2002) 839–843, https://doi.org/10.1007/S00247-002-0825-1.

[47] B. Nigro, C. Grimaldi, M.A. Miller, P. Ryser, T. Schilling, Tunneling conductivity in composites of attractive colloids, J. Chem. Phys. 136 (2012), 164903, https://doi.org/10.1063/1.4705307.

[48] A.B. Oskouyi, U. Sundararaj, P. Mertiny, Tunneling conductivity and piezoresistivity of composites containing randomly dispersed conductive nano-platelets, Materials 7 (2014) 2501, https://doi.org/10.3390/MA7042501.

[49] A.C. da Silva, S.I. Córdoba de Torresi, Advances in conducting, biodegradable and biocompatible copolymers for biomedical applications, Front Mater 6 (2019) 98, https://doi.org/10.3389/FMATS.2019.00098.

[50] C.J. Bettinger, Recent advances in materials and flexible electronics for peripheral nerve interfaces, Bioelectronic Medicine 4 (2018) 1, https://doi.org/10.1186/S42234-018-0007-6, 4 (2018) 1–10.

[51] A. Boongird, N. Nasongkla, S. Hongeng, N. Sukdawong, W. Sa-Nguanruang, N. Larbcharoensub, Biocompatibility study of glycofurol in rat brains (2011) 77–83, https://doi.org/10.1258/EBM.2010.010219.

[52] D. Allhenn, A. Lamprecht, Microsphere preparation using the untoxic solvent glycofurol, Pharm. Res. (N. Y.) 28 (2011) 563–571, https://doi.org/10.1007/S11095-010-0304-6.

[53] S. Kirkpatrick, The nature of percolation 'channels, Solid State Commun. 12 (1973) 1279–1283, https://doi.org/10.1016/0038-1098(73)90865-X.

[54] S. Kirkpatrick, Percolation and conduction, Rev. Mod. Phys. 45 (1973) 574, https://doi.org/10.1103/RevModPhys.45.574.

[55] H.P. Wu, X.J. Wu, M.Y. Ge, G.Q. Zhang, Y.W. Wang, J.Z. Jiang, Effect analysis of filler sizes on percolation threshold of isotropical conductive adhesives, Compos. Sci. Technol. 67 (2007) 1116–1120, https://doi.org/10.1016/J.COMPSCITECH.2006.05.017.

[56] X. Jing, W. Zhao, L. Lan, The effect of particle size on electric conducting percolation threshold in polymer/conducting particle composites, J. Mater. Sci. Lett. 19 (2000) 377–379, https://doi.org/10.1023/A:1006774318019.

[57] S. Wu, A generalized criterion for rubber toughening: the critical matrix ligament thickness, J. Appl. Polym. Sci. 35 (1988) 549–561, https://doi.org/10.1002/APP.1988.070350220.

[58] L. Efthymiou, G. Camuso, G. Longobardi, T. Chien, M. Chen, F. Udrea, On the source of oscillatory behaviour during switching of power enhancement mode GaN HEMTs, Energies 10 (2017) 407, https://doi.org/10.3390/en10030407.

[59] R.A. Rakkesh, D. Durgalakshmi, P. Karthe, S. Balakumar, Role of interfacial charge transfer process in the graphene-ZnO-MoO3 core-shell nanoassemblies for efficient disinfection of industrial effluents, Processing and Application of Ceramics 13 (2019) 376–386, https://doi.org/10.2298/PAC1904376A.

[60] N. Li, H. Teng, L. Zhang, J. Zhou, M. Liu, Synthesis of Mo-doped WO 3 nanosheets with enhanced visible-light-driven photocatalytic properties, RSC Adv. 5 (2015) 95394–95400, https://doi.org/10.1039/C5RA17098B.

[61] J.J. Duffy, M. Panalytical, A.J. Hill, Suspension Stability; Why Particle Size, Zeta Potential and Rheology Are Important, TRANSACTIONS OF THE NORDIC RHEOLOGY SOCIETY, 2012, p. 20. https://www.researchgate.net/publication/279851764. accessed October 10, 2022.

[62] A.R.I. Ali, B. Salam, A review on nanofluid: preparation, stability, thermophysical properties, heat transfer characteristics and application, SN Appl. Sci. 2 (2020) 1–17, https://doi.org/10.1007/S42452-020-03427-1.

[63] Matthias Weil, Wolf-Dieter Schubert, The Beautiful Colours of Tungsten Oxides, International Tungsten Industry Association, 2013. https://www.semanticscholar.org/paper/The-Beautiful-Colours-of-Tungsten-Oxides-Weil-Schubert/c477efb0be273f9ab630401ca6f47e7514dc1dde. accessed October 10, 2022.

[64] E. Patrick, M.E. Orazem, J.C. Sanchez, T. Nishida, Corrosion of tungsten microelectrodes used in neural recording applications, J. Neurosci. Methods 198 (2011) 158–171, https://doi.org/10.1016/J.JNEUMETH.2011.03.012.

[65] R. Buchwald, M.D. Breed, A.R. Greenberg, The thermal properties of beeswaxes: unexpected findings, J. Exp. Biol. 211 (2008) 121–127, https://doi.org/10.1242/jeb.007583.

[66] N.E. Aranda-Ledesma, I. Bautista-Hernández, R. Rojas, P. Aguilar-Zárate, N. del P. Medina-Herrera, C. Castro-López, G.C. Guadalupe Martínez-Ávila, Candelilla wax: prospective suitable applications within the food field, Lebensm. Wiss. Technol. 159 (2022), https://doi.org/10.1016/J.LWT.2022.113170.
[67] M. Chichakli, F.W. Jessen, Crystal morphology in hydrocarbon systems, Ind. Eng. Chem. 59 (1967) 86–98, https://doi.org/10.1021/ie50689a009.
[68] F. Fratini, G. Cilia, B. Turchi, A. Felicioli, Beeswax: a minireview of its antimicrobial activity and its application in medicine, Asian Pac J Trop Med 9 (2016) 839–843, https://doi.org/10.1016/J.APJTM.2016.07.003.
[69] A.P. Tulloch, Beeswax—composition and analysis, Bee World 61 (1980) 47–62, https://doi.org/10.1080/0005772x.1980.11097776.
[70] M. Miyauchi, M. Shibuya, Z.-G. Zhao, Z. Liu, Surface wetting behavior of a WO 3 electrode under light-irradiated or potential-controlled conditions, J. Phys. Chem. C 113 (2009) 10642–10646, https://doi.org/10.1021/jp901097b.
[71] L.H. Liang, X.M. You, H.S. Ma, Y.G. Wei, Interface energy and its influence on interface fracture between metal and ceramic thin films in nanoscale, J. Appl. Phys. 108 (2010), https://doi.org/10.1063/1.3501090.
[72] X. Pang, L. Zhang, H. Yang, K. Gao, A.A. Volinsky, Residual stress and surface energy of sputtered TiN films, J. Mater. Eng. Perform. 24 (2015) 1185–1191, https://doi.org/10.1007/S11665-015-1393-5.
[73] K. Szymczyk, A. Zdziennicka, J. Krawczyk, B. Jańczuk, Wettability, adhesion, adsorption and interface tension in the polymer/surfactant aqueous solution system: II. Work of adhesion and adsorption of surfactant at polymer-solution and solution-air interfaces, Colloids Surf. A Physicochem. Eng. Asp. 402 (2012) 139–145, https://doi.org/10.1016/J.COLSURFA.2012.02.055.
[74] Y. Wang, C.J. Hansen, C.C. Wu, E.J. Robinette, A.M. Peterson, Effect of surface wettability on the interfacial adhesion of a thermosetting elastomer on glass, RSC Adv. 11 (2021) 31142–31151, https://doi.org/10.1039/D1RA05916E.
[75] International Organization for Standardization, Biological evaluation of medical devices — Part 12: Sample preparation and reference materials, ISO 10993-12: 2021. 5 (2021) 1-21, https://www.iso.org/standard/75769.html, accessed January 04, 2023.
[76] X. Wei, B. Liu, G. Liu, F. Yang, F. Cao, X. Dou, W. Yu, B. Wang, G. Zheng, L. Cheng, Z. Ma, Y. Zhang, J. Yang, Z. Wang, J. Li, D. Cui, W. Wang, H. Xie, L. Li, F. Zhang, W.C. Lineaweaver, D. Zhao, Mesenchymal stem cell-loaded porous tantalum integrated with biomimetic 3D collagen-based scaffold to repair large osteochondral defects in goats, Stem Cell Res. Ther. 10 (2019) 1–17, https://doi.org/10.1186/S13287-019-1176-2.
[77] J. Sun, L. Li, F. Xing, Y. Yang, M. Gong, G. Liu, S. Wu, R. Luo, X. Duan, M. Liu, M. Zou, Z. Xiang, Graphene oxide-modified silk fibroin/nanohydroxyapatite scaffold loaded with urine-derived stem cells for immunomodulation and bone regeneration, Stem Cell Res. Ther. 12 (2021) 1–20, https://doi.org/10.1186/s13287-021-02634-w.
[78] X. Tang, Y. Khan, C.T. Laurencin, Biomimetic electroconductive scaffolds for muscle regenerative engineering, Adv. Mater. Lett. 8 (2017) 587–591, https://doi.org/10.5185/AMLETT.2017.7106.
[79] S.A. Riboldi, M. Sampaolesi, P. Neuenschwander, G. Cossu, S. Mantero, Electrospun degradable polyesterurethane membranes: potential scaffolds for skeletal muscle tissue engineering, Biomaterials 26 (2005) 4606–4615, https://doi.org/10.1016/J.BIOMATERIALS.2004.11.035.
[80] H.A. Rather, R. Thakore, R. Singh, D. Jhala, S. Singh, R. Vasita, Antioxidative study of Cerium Oxide nanoparticle functionalised PCL-Gelatin electrospun fibers for wound healing application, Bioact. Mater. 3 (2018) 201–211, https://doi.org/10.1016/J.BIOACTMAT.2017.09.006.
[81] M. Kacániová, N. Vuković, R. Chlebo, P. Haščík, K. Rovná, J. Cubon, M. Dzugan, A. Pasternakiewicz, The antimicrobial activity of honey, bee pollen loads and beeswax from Slovakia, Arch. Biol. Sci. 64 (2012) 927–934, https://doi.org/10.2298/ABS1203927K.
[82] N.B. Ghanem, The antimicrobial activity of some honey bee products and some Saudi folkloric plant extracts, J. King Abdulaziz Univ. Sci. 23 (2011) 47–62, https://doi.org/10.4197/sci.23-2.4.
[83] Y.M. Pogosyan, T. v Khanamiryan, A.Y. Pogosyan, E.K. Avetisyan, S.S. Burnazyan, Study of biodegradable properties of beeswax membrane in the focus of ectopic implantation, BALKAN JOURNAL OF STOMATOLOGY 15 (2011) 142–149.
[84] T. Rubic-Schneider, M. Kuwana, B. Christen, M. Aßenmacher, O. Hainzl, F. Zimmermann, R. Fischer, V. Koppenburg, S.D. Chibout, T.M. Wright, A. Seidl, M. Kammüller, T-cell assays confirm immunogenicity of tungsten-induced erythropoietin aggregates associated with pure red cell aplasia, Blood Adv 1 (2017) 367, https://doi.org/10.1182/BLOODADVANCES.2016001842.
[85] M.P. Grant, C.R. Vanderschee, H. Chou, A. Bolt, L.M. Epure, D. Kuter, J. Antoniou, S. Bohle, K.K. Mann, F. Mwale, Tungsten accumulates in the intervertebral disc and vertebrae stimulating disc degeneration and upregulating markers of inflammation and pain, Eur. Cell. Mater. 41 (2021) 517–530, https://doi.org/10.22203/ECM.V041A33.
[86] R. Lemus, C.F. Venezia, An update to the toxicological profile for water-soluble and sparingly soluble tungsten substances, Crit. Rev. Toxicol. 45 (2015) 388–411, https://doi.org/10.3109/10408444.2014.1003422.
[87] E. Lassner, W. Schubert, Tungsten Properties, Chemistry, Technology of the Element, Alloys, and Chemical Compounds, Kluwer Academic/Plenum Publishers, 1999, https://doi.org/10.1007/978-1-4615-4907-9.
[88] P.M. Radcliffe, T.L. Leavens, D.J. Wagner, A.O. Olabisi, M.F. Struve, B.A. Wong, E. Tewksbury, G.D. Chapman, D.C. Dorman, Pharmacokinetics of radiolabeled tungsten (188W) in male Sprague-Dawley rats following acute sodium tungstate inhalation, Inhal. Toxicol. 22 (2009) 69–76, https://doi.org/10.3109/08958370902913237.
[89] S. Chinde, N. Dumala, M.F. Rahman, S. Srinivas, K. Kamal, S.I. Kumari, M. Mahboob, P. Grover, Toxicological assessment of tungsten oxide nanoparticles in rats after acute oral exposure, Environ. Sci. Pollut. Control Ser. 24 (2017) 13576–13593, https://doi.org/10.1007/s11356-017-8892-x.
[90] J.P. Goullé, L. Mahieu, J. Castermant, N. Neveu, L. Bonneau, G. Lainé, D. Bouige, C. Lacroix, Metal and metalloid multi-elementary ICP-MS validation in whole blood, plasma, urine and hair: reference values, Forensic Sci. Int. 153 (2005) 39–44, https://doi.org/10.1016/J.FORSCIINT.2005.04.020.

Glossary

ASTM: American Society for Testing and Materials
ADC: analog-to-digital converter
BSE: backscattered electron
C: carbon
CBC: complete blood count
CP: conductive polymer
DSC: differential scanning calorimetry
DMEM: Dulbecco's Modified Eagle Medium
ELISA: enzyme-linked immunosorbent assay
EDS: energy-dispersive X-ray spectroscopy
EthD-1: ethidium homodimer-1
EDTA: ethylenediaminetetraacetic acid
FBS: fetal bovine serum
FIB: focused ion-beam
FRA: frequency response analyzer
GF: glycofurol
H&E: hematoxylin and eosin
ICP-MS: Inductively coupled plasma mass spectrometry
ISO: International Standards Organization
Mg: magnesium
Mo: molybdenum
PS: penicillin–streptomycin
PBS: phosphate-buffered saline
PBTPA: poly butanedithiol 1,3,5-triallyl-1,3,5-triazine-2,4,6(1H,3H,5H)-trione pentenoic anhydride
PEDOT: poly(3,4-ethylenedioxythiophene)
PDMS: polydimethylsiloxane
PI: polyimide
PLGA: poly(lactide–co–glycolide)
PPy: polypyrrole
RF: radio frequency
SEM: scanning electron microscopy
Si: silicon
Ag: silver
Sn: tin
W: tungsten
UV: ultraviolet;
UTM: universal test machine
WBC: white blood cell
XPS: X-ray photoelectron spectroscopy